Simulated QLCS Vortices in a High-Shear, Low-CAPE Environment🖉

Levi T. Lovell[a] and Matthew D. Parker[a]

[a] *Department of Marine, Earth, and Atmospheric Sciences, North Carolina State University, Raleigh, North Carolina*

ABSTRACT: Tornadoes produced by quasi-linear convective systems (QLCSs) in low instability environments present distinctive challenges for forecasters. This study analyzes a population of 56 vortices (all cyclonic) in a full-physics, case study simulation to examine vortex characteristics and their relationships to the pre-line environment. Peak surface vortex intensity correlates with peak vortex depth, peak surface wind speed, and vortex pathlength. The strongest vortices are the deepest and longest lived, implying that they would be most detectable. The modeled surface vortices are primarily associated with gust front cusps and bow echoes, line breaks, and supercell-like features. Strong vortices frequently have sustained, superposed surface vorticity and near-ground updrafts for several minutes. Although weak vortices lack this superposition, they often exhibit impressive midlevel vorticity and midlevel updrafts. The environments of the weak and strong vortices are similar with small, yet statistically significant, differences in several thermodynamic and kinematic fields. The profiles near strong vortices have more low-level CAPE, steeper lapse rates, and stronger deep-layer vertical wind shear. However, the small magnitudes of the differences imply that forecasters might struggle to discriminate well between nontornadic and tornadic environments in high-shear, low-CAPE events. Despite the similarities, the profiles produce distinct reflectivity, updraft, and vertical vorticity distributions in idealized cloud model simulations. The most intense updrafts and vortices in the idealized runs occur when the environmental profiles from the strong vortex cases are combined with a QLCS orientation more normal to the lower-tropospheric vertical wind shear.

KEYWORDS: Tornadoes; Convective storms; Storm environments; Large eddy simulations; Mesoscale models

1. Introduction

A wide range of thermodynamic and kinematic environments can produce severe weather (damaging winds, tornadoes, and hail). Convective storms that occur in high-shear, low-CAPE (HSLC) environments have historically received less attention than those in high-shear, high-CAPE environments despite their commonality in the United States (Dean and Schneider 2008). HSLC convection frequently occurs during the cool season and nighttime hours when situational awareness can be low (Smith et al. 2008; Sherburn and Parker 2014; Sherburn et al. 2016). Considerable overlap also exists between the HSLC severe event climatology in the southeastern U.S. and populations with fewer resources and less durable structures (Strader and Ashley 2018). Additionally, population increases and sprawl compound socioeconomic vulnerabilities (Ashley and Strader 2016). Such factors likely contribute to a higher percentage of deadly tornadoes in the Southeast (3.8%) than across the entire United States (2.0%; Anderson-Frey et al. 2019). Convection in HSLC environments is notoriously shallow, and radar-detectable signatures of rotation are only visible at close range from a WSR-88D (Davis and Parker 2014). These factors contribute to lower tornado warning skill with a higher false alarm rate (FAR) and a lower probability of detection (POD) in HSLC tornado watches (Dean and Schneider 2008; Anderson-Frey et al. 2016).

Quasi-linear convective systems (QLCSs) account for approximately 12% of tornadoes in the United States, 18% of tornadoes in the Southeast, and 23% of HSLC tornadoes in the Southeast (Anderson-Frey et al. 2019). Mesogamma-scale surface vortices within QLCSs (i.e., mesovortices) can also play a critical role in producing severe straight-line winds, so an enhanced understanding of vortex character and formation is an important research problem. Some of the first QLCS observational studies noted damage swaths associated with mesovortices and tornadoes near and just north of the apex of bow echoes (Przybylinski 1995; Funk et al. 1999). Tornadic mesovortices are also more likely to occur near a strong rear-inflow jet and have significantly longer life spans than nontornadic mesovortices (Atkins et al. 2004). Superposition of a descending rear-inflow jet on the southern side of cyclonic mesovortices may further contribute to intense, damaging winds (Wakimoto et al. 2006; Wheatley et al. 2006). Such studies have relied heavily on post-event damage surveys, leaving a need for more information about the vortices themselves.

Recent modeling studies augment the observational work and allow controlled investigation of vortex characteristics and dynamics, resulting in several hypothesized vortex-genesis mechanisms. Cyclonic–anticyclonic couplets of vortices can be produced via tilting of system-generated vortex lines either downward (Trapp and Weisman 2003; Wakimoto et al. 2006) or upward (Atkins and Laurent 2009b). Cyclonic-only vortices could be produced via tilting of baroclinically generated streamwise vorticity (Atkins and Laurent 2009b), tilting of frictionally generated vorticity (Schenkman et al. 2012; Xu et al. 2015), or release of horizontal shearing instability (Carbone

1982; Wakimoto and Wilson 1989; Lee and Wilhelmson 1997; Wheatley and Trapp 2008; Conrad and Knupp 2019). In addition, Flournoy and Coniglio (2019) identified multiple sources of mesovortex parcels, with contributions to rotation from rain-cooled outflow parcels (streamwise vorticity) and warm inflow parcels (crosswise vorticity). Interactions between cold pool intensity and low-level environmental shear may also influence mesovortex genesis and maintenance (Rotunno et al. 1988; Atkins and Laurent 2009a; Schaumann and Przybylinski 2012). In short, there remains no unified theory for the formation and maintenance of mesovortices within linear convective systems.

The primary goal of the present study is to investigate the effect of environmental heterogeneities on small-scale vortex structure and production within HSLC linear convection. We examine a large population of vortices from a single case to determine whether detectable signals (either within the environment or within the QLCS itself) presage mesovortex and severe weather production. We focus on simulations of an observed HSLC QLCS with periods of both prolific tornado production and nonproduction. Are such differences primarily related to internal storm-scale processes or the pre-convective inflow environment? To answer this, we employ a hierarchy of models to characterize vortex structures, evolution, and near-inflow environments for an ensemble of simulated vortices.

Section 2 is a review of the data and methods used in the study, including case study selection and model configuration. Section 3 provides an analysis of vortex statistics, including relationships between environmental parameters and vortex characteristics. Section 4 describes the pre-storm environments near null and vortex events. Section 5 examines the impacts of the pre-storm environments via idealized simulations using composite profiles. Section 6 is a summary of the results, conclusions, operational implications, and future work.

2. Methods

a. Case study selection

After generating an extensive list of HSLC QLCS events from 2015 to 2019 in the United States (in environments with less than 1000 J kg^{-1} mixed-layer CAPE (MLCAPE) and more than 18 m s^{-1} of 0–6-km bulk wind difference (BWD), occurring from mid-October to mid-April each cool season), we selected the 24–25 February 2018 QLCS for closer study. In addition to representing the attributes of the entire case database well (e.g., instability, shear, location, and timing), the QLCS was impactful, resulting in 2 fatalities, 23 injuries, and nearly $25 million (U.S. dollars) in damages. The event also consisted of an early period with 0 QLCS tornado reports[1] as well as a late period with 31 tornado reports, including 6 of EF2 intensity. The dichotomy in production facilitated our focus on the roles of the environment versus within-storm processes on nontornadic and tornadic QLCS vortices. Notably, 22 of the 78 severe wind reports produced

by the QLCS occurred during the early nontornadic period, suggesting that surface-based, severe convection was present throughout the event.

On 24 February 2018, a semi-persistent longwave trough was present across the western United States with an embedded, fast-moving shortwave trough (Figs. 1a,b). A surface low pressure system formed in central Texas on the morning of 24 February and moved northeastward into southern Missouri during the afternoon (Figs. 1c,d). Storms formed and began to grow upscale (interested readers can look ahead to the radar summaries in Fig. 4) near the cold front during the early afternoon in Oklahoma and Arkansas. An observed sounding from Little Rock, Arkansas (LZK), at 2000 UTC depicted a robust HSLC convective environment with 580 J kg^{-1} of MLCAPE and 36 m s^{-1} of 0–6-km vertical wind shear (Fig. 2a). Notably, although the QLCS was maturing at this time, there were no tornado reports (i.e., only damaging wind reports) in Arkansas from 1800 to 2300 UTC. At 2311 UTC, the QLCS produced its first tornado in northeastern Arkansas, with many subsequent tornadoes in Missouri, Tennessee, Kentucky, and Ohio. The nearest observed sounding to these events from Nashville, Tennessee (BNA), at 0000 UTC depicted a drier, less favorable environment with 165 J kg^{-1} of MLCAPE and 33 m s^{-1} of 0–6-km vertical wind shear (Fig. 2b). However, BNA was more than 250 km downstream of the convection and likely unrepresentative of the immediate pre-line environment at this time. The SPC Mesoscale Analysis (SFCOA; Bothwell et al. 2002) fields of MLCAPE[2] and 0–6-km vertical wind shear (not shown) suggest that the instability was declining throughout the tornadic phase while the deep-layer vertical wind shear was increasing. Overall, this case study provides a unique opportunity to assess the roles of the environment and within-storm processes on the rather abrupt increase in QLCS tornado production.

b. Numerical simulations

While the 24–25 February 2018 case is pertinent to our research questions, there are not sufficiently detailed observations to accomplish our goals. For this reason, we utilized a hierarchy of model simulations as a proxy. A similar two-pronged approach was successfully employed by Parker et al. (2020) and Parker (2021) to investigate a convective system in multiple modeling frameworks of differing complexity.

We first ran a "real-world" full-physics case study simulation using the fully compressible, nonhydrostatic Advanced Research version of the Weather Research and Forecasting (WRF) Model (WRF-ARW; Skamarock et al. 2019). The real-data, full-physics WRF simulation more completely and realistically depicts the observed events with horizontal heterogeneity and fully evolving large-scale features. However, this realism comes at a cost—the abundance of parameterizations

---

[1] Four tornadoes associated with an isolated supercell were reported in Tennessee and Kentucky before 2330 UTC.

[2] According to the objective surface analyses, MLCAPE only exceeded 1000 J kg^{-1} along a corridor from central Louisiana to southeastern Arkansas to northern Mississippi before 2100 UTC. All tornadoes occurred between 2317 and 0550 UTC when MLCAPE was well below the 1000 J kg^{-1} threshold.
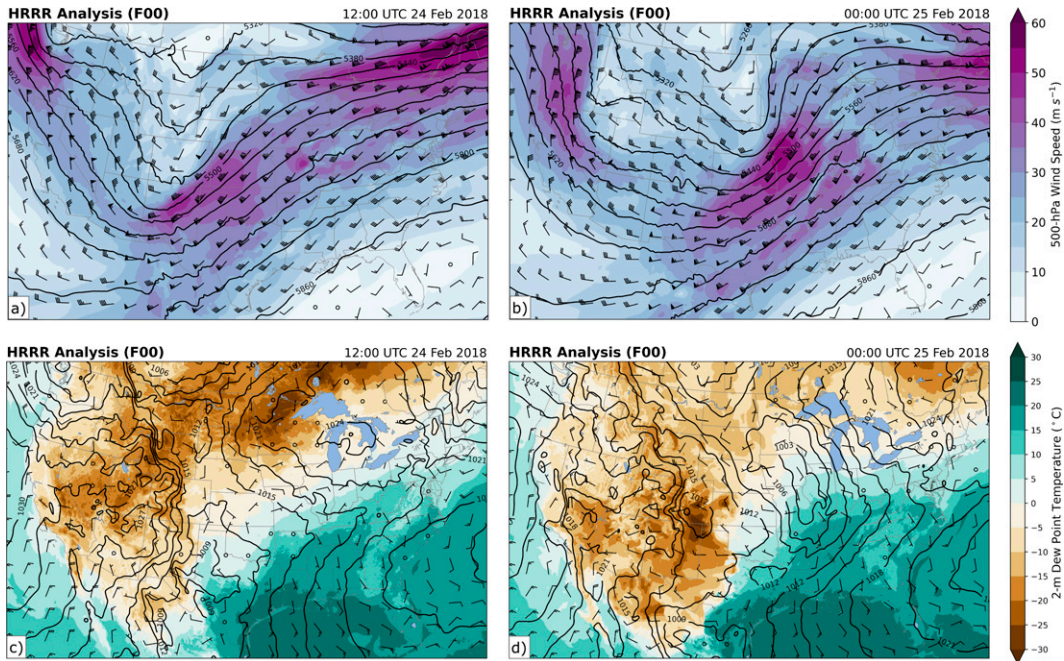
FIG. 1. 500-hPa heights (black contour; m), 500-hPa wind speed (shading; m s^{-1}), and 500-hPa wind (barbs; m s^{-1}) valid at (a) 1200 UTC 24 Feb 2018 and (b) 0000 UTC 25 Feb 2018 via HRRR analyses. Surface MSLP (black contour; hPa), 2 m AGL dewpoint temperature (shading; °C), and 10-m wind (barbs; m s^{-1}) valid at (c) 1200 UTC 24 Feb 2018 and (d) 0000 UTC 25 Feb 2018 via HRRR analyses. Note: Wind barbs depicted in m s^{-1} with each barb and flag representing 5 and 25 m s^{-1}, respectively.

can complicate the interpretation of results, and the constraints of large-scale balance mean that only limited kinds of environmental sensitivities can be tested. Therefore, we also conducted a qualitative assessment of HSLC linear convection and vortex behaviors in a suite of simulations performed in an idealized modeling framework using Cloud Model 1 (CM1; Bryan and Fritsch 2002). By eliminating large-scale evolution and parameterizations of the radiative, boundary layer, and surface layer processes, the idealized model reveals how convection responds specifically to the local environment. In effect, these simulations address whether the near-inflow environmental profiles from the WRF simulation(s) possess sufficient information to determine the number and intensity of potentially tornadic QLCS vortices.

Increasingly, with modern computing power, ensembles of simulations provide ranges of possible outcomes and quantification of uncertainty. Whereas large climatological studies typically compare "hits" and "nulls" across many events in very different environments, our approach focuses on the details of a population of vortices that occur in a single QLCS within ostensibly similar synoptic and mesoscale environments. Such an analysis more closely emulates the challenges ("to warn or not to warn") faced by a forecaster on a given day.

1) WRF MODEL CONFIGURATION

The full-physics, real-world simulations used version 4.0 of the WRF-ARW Model. The simulations included three nested grids (Table 1; Fig. 3). The 3-km domain was initialized

at 1200 UTC 24 February 2018 and run for 24 h with initial and lateral boundary conditions supplied by the High-Resolution Rapid Refresh (HRRR) model 0-h forecast fields from successive model runs. A one-way nested grid with 600-m grid spacing was run for 9 h, beginning at 1900 UTC 24 February 2018. It served as a conduit to two independent domains with 200-m grid spacing (labeled d03 and d04 in Fig. 3). The simulation on domain 3 began at 2000 UTC 24 February 2018 while the simulation on domain 4 began at 2200 UTC 24 February 2018. Each simulation ran for 5 h. The grid spacing on the finest mesh domains was sufficient to marginally resolve phenomena with horizontal length scales of 1–2 km, including QLCS mesovortices but excluding tornadoes themselves. We strategically placed these domains to capture the convective-scale evolution within the distinctly nontornadic and tornadic regimes. The physical parameterizations are summarized in Table 1, with convective motions treated explicitly on all grids. The large-eddy-permitting 200-m domains have slightly different physics and dynamics configurations (i.e., no PBL scheme) than the parent domains. For the innermost domains, we implemented the recommendations for running WRF large-eddy simulations by Dudhia (2014).

The WRF simulations presented herein effectively represent downscaled HRRR analyses with hourly updates to the lateral boundary conditions to ensure the model behavior closely represents the observations. The primary difference between the operational HRRR and the outer domain was the boundary layer scheme. Exact replication of the event was
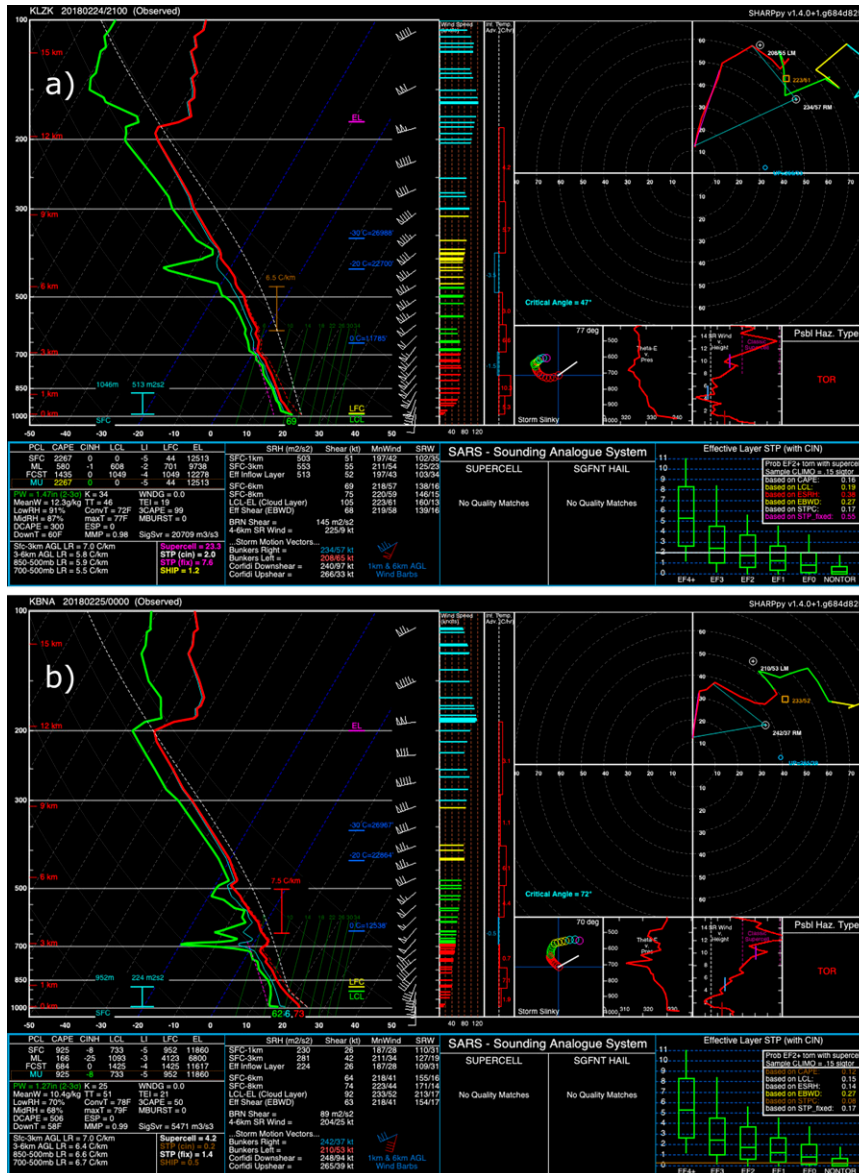
FIG. 2. Observed upper-air soundings from (a) Little Rock, AR (LZK), at 2000 UTC 24 Feb 2018 and (b) Nashville, TN (BNA), at 0000 UTC 25 Feb 2018 via SHARPpy.

never achievable, even with the highest-quality input data informing the solution. However, the overall system and environment evolution closely resemble the observations (Figs. 4 and 5).

We tested several other WRF setups with various microphysics schemes, radiation schemes, boundary layer schemes, and land surface schemes to examine model configuration sensitivity. The Thompson microphysics scheme produced the most realistic QPF swaths compared to the Morrison and WRF single-moment 6-class microphysics schemes. The RUC land surface model (LSM) produced low-level thermodynamic and kinematic profiles that more closely resembled observed soundings than the Noah LSM, which was consistently too dry. Radiation schemes did not significantly influence the evolution of the QLCS in our model setup tests.

2) CM1 MODEL CONFIGURATION

The idealized simulations were run using the CM1 model (Bryan and Fritsch 2002; Bryan and Morrison 2012), release 19. These simulations also used 200-m horizontal grid spacing but had far fewer parameterizations (Table 1) to complement the WRF via a simpler framework for attribution and isolation of physical processes. The primary focus of the CM1 simulations was on the role of the environment in producing QLCS behavior that is self-organized (Parker et al. 2020; Parker 2021). At initialization, each 3-h CM1 simulation consisted of a horizontally homogeneous model domain characterized by

TABLE 1. Summary of model settings for the WRF (v. 4.0) and CM1 (v. 19) simulations in this article. The colloquial names for various parameterizations are given in the table, with corresponding literature citations as follows: "Thompson microphysics scheme" (Thompson et al. 2008), "ACM2 boundary layer scheme" (Cohen et al. 2017), "RRTMG scheme" (Iacono et al. 2008), and "RUC scheme" (Benjamin et al. 2004).

Namelist option	WRF simulation	CM1 simulation
Δx, Δy	3–0.6–0.2 km, one-way nested	0.2 km
Vertical levels	50	120
Δz	Stretched, $\approx$25–500 m	Stretched, 50–200 m
Model top	$\approx$20 km	18 km
Microphysical parameterization	Thompson scheme	Thompson scheme
Turbulence parameterization	d01, d02: ACM2 scheme	TKE-based subgrid closure
	d03, d04: Smagorinsky first-order closure (3D)	
Radiation parameterization	RRTMG scheme	None
Land surface parameterization	RUC scheme	None, free-slip bottom boundary
Initialization	HRRR model analysis	Horizontally homogeneous (WRF profile) with inserted block of cool air
Lateral boundary conditions	HRRR model analyses every 1 h	Open radiative condition
Simulation time	d01: 24 Feb 1200 UTC for 24 h	3 h
	d02: 24 Feb 1900 UTC for 9 h	
	d03: 24 Feb 2000 UTC for 5 h	
	d04: 24 Feb 2200 UTC for 5 h	
Dynamical simplifications	None	Coriolis acceleration omitted

composite soundings (e.g., tornadic and nontornadic) obtained from the WRF simulation. We utilized WRF soundings instead of observed soundings because of their universal availability, and they also facilitated a more direct comparison between the CM1 and WRF results. For consistency with the WRF Model setup, the Thompson microphysics scheme was also implemented in the CM1 simulations.

Contrary to the WRF simulations that generated convection organically, the CM1 simulations initiated convection via a 3D cold anomaly near the surface intended to resemble linear forcing from an outflow boundary. Other initiation techniques (e.g., line of warm bubbles or updraft nudging) tended to less reliably produce sustained convection. The initial north–south-oriented cold pool in these simulations was characterized by a minimum potential temperature perturbation
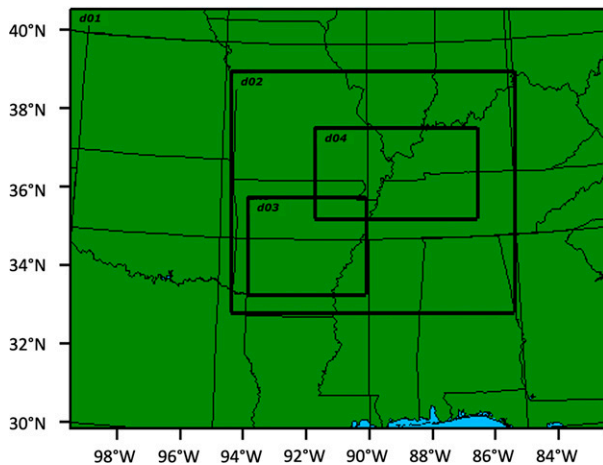

FIG. 3. WRF domain nest configuration with the 3-km domain (d01; image frame), 600-m domain (d02), 200-m "nontornadic" domain (d03), and 200-m "tornadic" domain (d04).

of -6 K at the surface, consistent with observations from regional airports (observed deficits ranged from $-4°$ to $-7°$C in the Little Rock and Nashville areas) and WRF Model output. At initialization, the "block" of relatively cool, dense air weakened with height up to 2.5 km (to 0-K perturbation) and extended the meridional length of the domain. Random potential temperature perturbations (± 0.5 K) were applied to the initial conditions to facilitate realistic, three-dimensional structures within the convection.

Vertical motion due to large-scale and mesoscale heterogeneity is notably absent in this idealized framework, so the sustained linear convection in this environment is effectively driven by a self-organizing process. These self-organizing convective processes produced deviations in the initial cold pool intensity, such that the starting anomaly acted only as a convective trigger. The two-pronged modeling approach enables synergy between qualitative analysis of the WRF's realistic case simulation and a more controlled assessment of the QLCS's sensitivities to the pre-convective environment.

c. Vortex identification

Vortices were identified by analyzing the Okubo–Weiss parameter (OW; Okubo 1970; Weiss 1991), which is negative where rotation dominates strain or deformation in the flow field:

$$OW = s_n^2 + s_s^2 - \zeta^2, \qquad (1)$$

where s_n is the normal strain component, s_s is the shear strain component, and ζ is the relative vertical vorticity:

$$s_n = \frac{\delta u}{\delta x} - \frac{\delta v}{\delta y}, \; s_s = \frac{\delta v}{\delta x} + \frac{\delta u}{\delta y}, \; \text{and} \; \zeta = \frac{\delta v}{\delta x} - \frac{\delta u}{\delta y}. \qquad (2)$$

The purpose of using OW instead of ζ for vortex identification is to isolate rotation (as opposed to shearing) in the flow
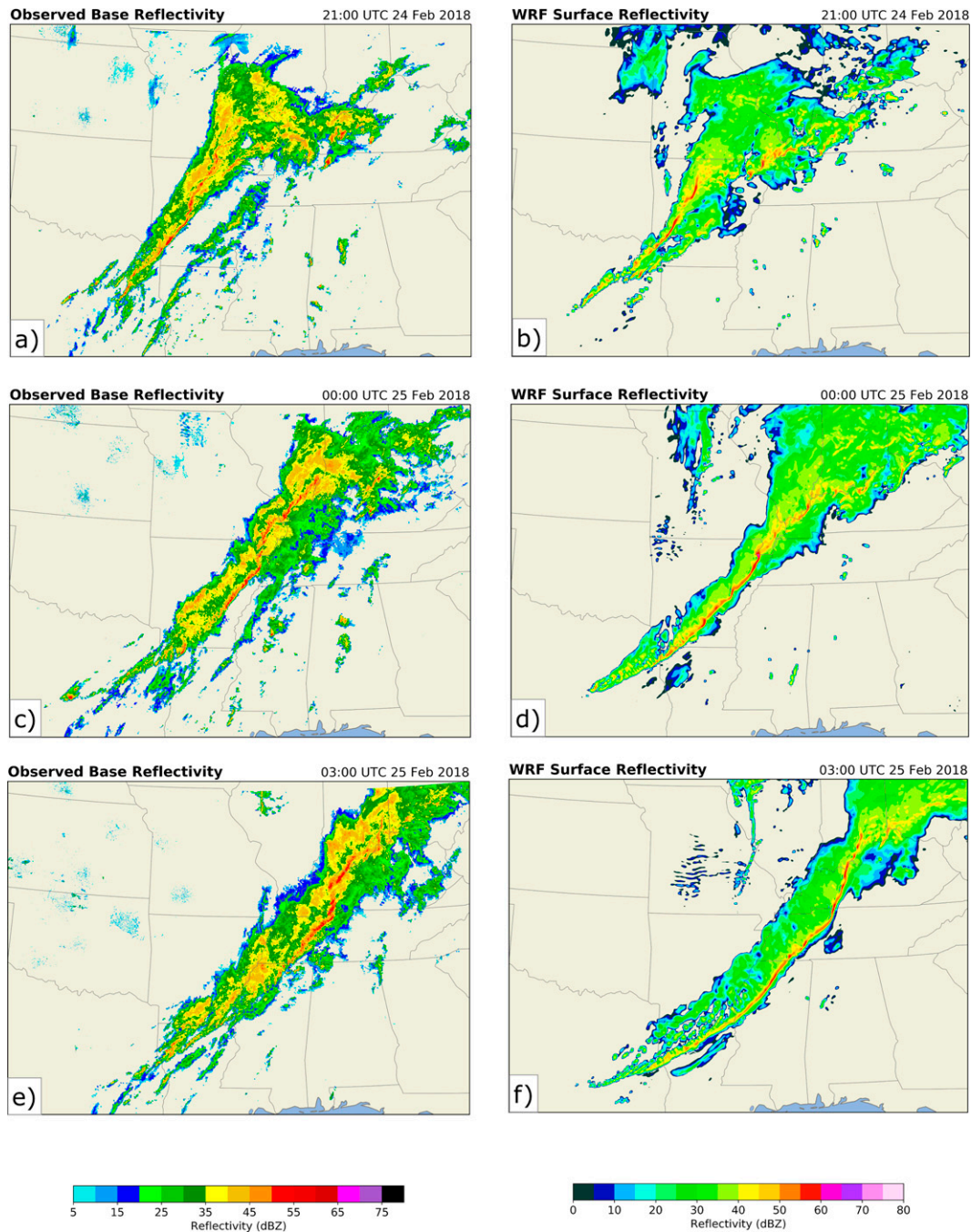
FIG. 4. (a),(c),(e) Observed base reflectivity and (b),(d),(f) WRF simulated surface reflectivity at (top) 2100 UTC 24 Feb 2018, (middle) 0000 UTC 25 Feb 2018, and (bottom) 0300 UTC 25 Feb 2018. Note: Simulated reflectivity on the outer domain (domain 1) is shown.

field. On the 200-m grids, a near-surface (25 m AGL) OW threshold of -0.01 s^{-2} was used to define each low-level vortex as in Coffer and Parker (2017), corresponding to a value of $|\zeta| = 0.1$ s^{-1} for pure rotation.

A vortex was defined as a contiguous region of points in the modeled surface OW field for which OW < -0.01 s^{-2} for at least two consecutive 1-min output times. If an existing vortex

failed to meet the threshold at one output time and later met the criteria again (i.e., dissipated and subsequently reformed), it was documented as the start of a new vortex track, not a continuation of the previous vortex track. We relaxed the continuity requirement to permit a 5-min gap for each vortex track (as long as the OW continued to exceed 50% of the threshold) to determine whether vortices might be overcounted
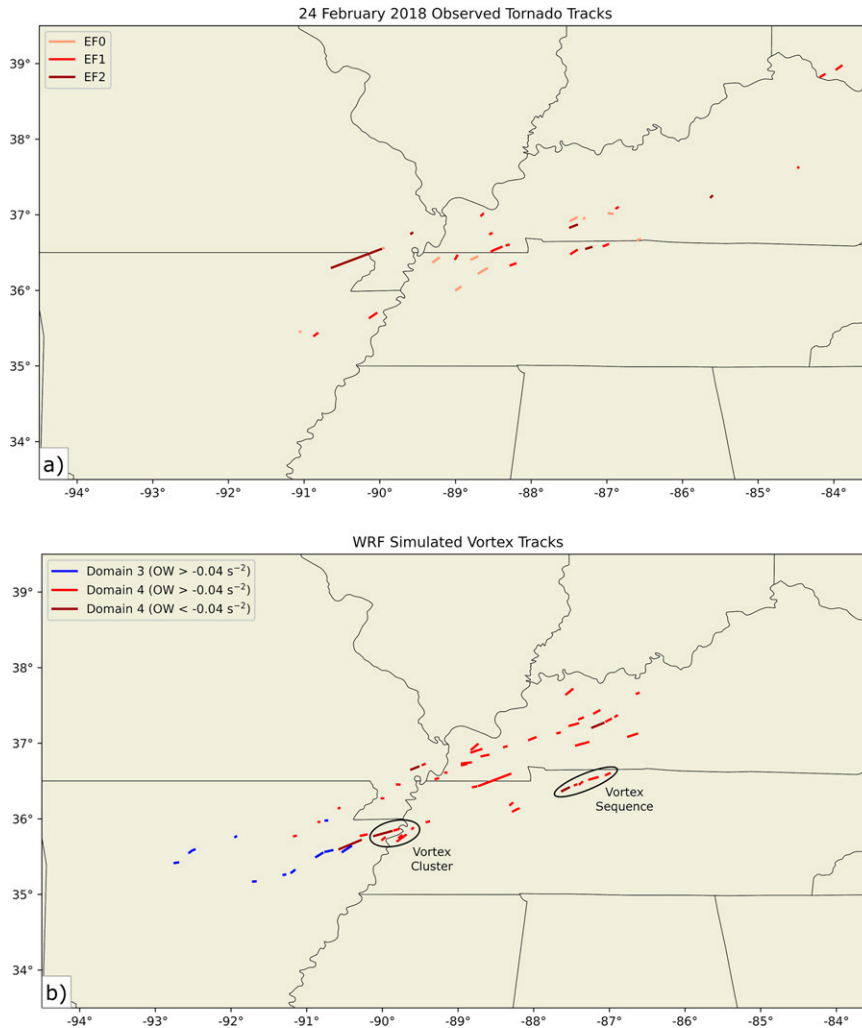
FIG. 5. (a) SPC observed tornado tracks with EF-scale ratings and (b) WRF simulated vortex tracks defined by Okubo–Weiss values less than -0.01 s^{-2}. Blue tracks indicate vortices in WRF domain 3 (Arkansas). Red tracks indicate vortices in WRF domain 4 (Kentucky/Tennessee). Dark red tracks indicate the most intense vortices defined by Okubo–Weiss values less than -0.04 s^{-2}. Note: Storm report data from NCEI Storm Events Database can be biased by non-uniform population distribution and reporting procedures across forecast offices.

by this method. As a result, the vortex count fell by 16%, but the median vortex statistics (e.g., OW, depth, wind speed, and duration) were relatively insensitive to this choice. Therefore, the first, simpler approach was retained.

Null events were identified using two independent approaches to create a robust comparison dataset of 31 events. The objective identification method involved the use of a "sub-tornadic" OW threshold (-0.0025 s^{-2}) at several vertical levels to identify weakly rotating areas at 500, 1000, and 3000 m AGL. This lower threshold produced a collection of rotating features that did not meet the original surface OW values required for vortex identification. Conversely, the subjective classification involved inspection of the surface reflectivity field to identify signatures like bow echoes, line breaks, or embedded supercell-like features. When

overlap existed between the approaches, we selected the objective method's locations for the analysis to avoid duplication.

Vortex intensity was assessed using the minimum OW value within each vortex. The nomenclature used in subsequent sections to describe vortices includes the following labels: "null," "weak," "strong," and "most intense." Minimum OW values greater than -0.01 s^{-2} are referred to as null (non-tornadic) events; minimum OW values between -0.01 and -0.0225 s^{-2} are referred to as weak vortices (36 events); minimum OW values between -0.0225 and -0.04 s^{-2} are referred to as strong vortices (15 events); minimum OW values less than -0.04 s^{-2} are referred to as the most intense vortices (5 events). The cutoffs correspond to $|\zeta| = 0.1$, 0.15, and 0.2 s^{-1}, respectively.

3. WRF-simulated QLCS vortices

The WRF simulation replicates the period from roughly 2100 to 2300 UTC in which the QLCS (Fig. 4b) produces very few, weak surface mesovortices (Fig. 5b; Arkansas), corresponding to the nontornadic phase of the observed case (Figs. 4a, 5a). It also replicates the period from roughly 2300 to 0300 UTC in which the QLCS (Figs. 4d,f) produces many surface mesovortices (Fig. 5b; Kentucky/Tennessee), corresponding to the tornadic phase of the observed case (Figs. 4c,e; Fig. 5a).

a. Statistics

Between the two 200-m domains, 56 (d03: 11, d04: 45) vortices meet the criteria outlined in section 2e. Each of the 56 vortex tracks comprises at least two consecutive output times; we refer to each of these 1-min snapshots as a vortex "point." Across both 200-m grids, there are 309 vortex points. Both vortex clusters and sequences exist in the simulated vortex tracks (Fig. 5b), indicating periods with multiple distinct vortices near one another as well as periods with repeated surface vortex-genesis events along a consistent path or trajectory. An analysis of all 309 vortex points reveal that the majority of vortices are weak[3] most of the time. Vortex depth is determined by obtaining the maximum height where OW ≤ -0.0025 s^{-2} within a vertical cross section aligned with the tilt of each vortex. The average vortex depth is 1498 m, and the median vortex depth is 1358 m.

Vortex tilt direction is variable among the population, ranging from south-southeast–north-northwest to northwest–southeast, with more than 70% of the vortices tilted toward the east, east-northeast, or northeast at the time of maximum depth along each track. Vortex characteristics (e.g., intensity and duration) are not strongly modulated by vortex tilt direction. Vortex tilt magnitude is quantified by the horizontal displacement of each vortex center with height (e.g., the distance between OW minima at 0 and 500 m, 0 and 1000 m, 0 and 2000 m, 0 and 3000 m). Vortices exhibit a tilt of nearly 45° in the lowest 500 m, but become less tilted with height (37° tilt in the lowest 1000 m, 29° tilt in the lowest 2000 m, and 23° tilt in the lowest 3000 m). The strong and weak vortices have no statistically significant differences in tilt over any of the layers tested (see Fig. S1 in the online supplemental material).

A time series of average OW throughout vortex life cycles (see Fig. S2) suggests peak intensity is transient and abrupt. Across the population of vortices, the aggregated OW value at peak intensity is 25%–30% higher than the aggregated OW values immediately preceding or succeeding it (i.e., at $t - 1$ min and $t + 1$ min). In contrast, there is less than 10% variance in vortex depth within 2 min of peak intensity, ranging from 1522 to 1664 m.

Because many of the vortex points correspond to weaker parts of each vortex's life cycle, the peak values from the 56 vortex tracks (Fig. 6) provide a more meaningful representation of the likely impact of each vortex. The distribution of

maximum vortex intensity (Fig. 6a) is left skewed with many weak vortices and only a few intense vortices, resulting in a mean OW value of -0.024 s^{-2} ($\zeta = 0.5$ s^{-1}) and a median OW value of -0.020 s^{-2} ($\zeta = 0.4$ s^{-1}). The vortex depth distribution (Fig. 6b) is slightly right-skewed with a large range from 525 to 3769 m. The distributions of vortex event duration and pathlength (Figs. 6c,d) are strongly right-skewed, with the majority of vortex events lasting fewer than 4 min and less than 7 km, respectively. The average duration is larger than the median duration (4.5 min versus 3.0 min) due to several impressive vortices that lasted 14, 17, and 20 min. The distribution of vortex motion speeds (Fig. 6e) is nearly normal, and, on average, the vortices moved at 24.7 m s^{-1}. However, vortex motion ranges from 12 to 38 m s^{-1}, indicative of significant forward speed variability within the convective system. While the variance is primarily attributed to changes in overall QLCS motion over time, vortex intensity and local gust front speed also contribute to the variation. The distribution of maximum near-surface wind speeds (Fig. 6f) is nearly normally distributed with a mean of 35.6 m s^{-1} and a median of 37.2 m s^{-1}. The near-surface wind speed maximum is displaced rightward of the vortex motion (i.e., south or southeast) in more than 90% of events. These wind speeds could correspond to significant severe wind reports (i.e., winds > 33 m s^{-1}). By comparison, the subset of nontornadic events has a median near-surface peak wind speed of 23.9 m s^{-1}.

It is worth asking whether the vortices of the greatest societal concern (i.e., strongest in terms of winds and OW) are generally the deepest or longest-lived, which would imply easier radar detection in operational scenarios. Relationships do exist between some of these metrics, as assessed via Spearman rank-order correlation coefficients (Fig. 7). The maximum near-surface wind speed is well correlated with peak intensity ($\rho = -0.74$), vortex motion speed ($\rho = 0.71$), and pathlength ($\rho = 0.69$).[4] These relationships suggest that the resultant near-surface wind speeds are a result of contributions from both the "background" flow within the cold pool (motion and pathlength) and rotation associated with the vortex (OW). Storm-scale rotation (i.e., rotational velocity) is also strongly correlated with peak intensity ($\rho = -0.81$; not shown), and 15 vortices surpassed the 20 m s^{-1} rotational velocity threshold established by Wurman and Kosiba (2013) for vortex classification as a tornado. Maximum surface wind speed is also moderately correlated with maximum vortex depth ($\rho = 0.54$), suggesting stronger vortices tend to be deeper and weaker vortices tend to be shallower. For most vortices, the maximum depth and maximum surface intensity occur within about two minutes of each other, so the vertical extent of a vortex may be a useful radar signature even if the near-surface circulation is below base scan height.

The most intense vortices, defined here as OW < -0.04 s^{-2} ($|\zeta| > 0.2$), have 61% greater maximum depth (3000 m) than the rest of the vortex population (1863 m). They also have a 170% longer pathlength (16.9 versus 6.1 km) and 167% longer

---

[3] 243 of the 309 vortex points had a minimum OW between -0.01 and -0.0225 s^{-2}.

[4] Vortex path length is expectedly strongly correlated with vortex duration ($\rho = 0.96$).
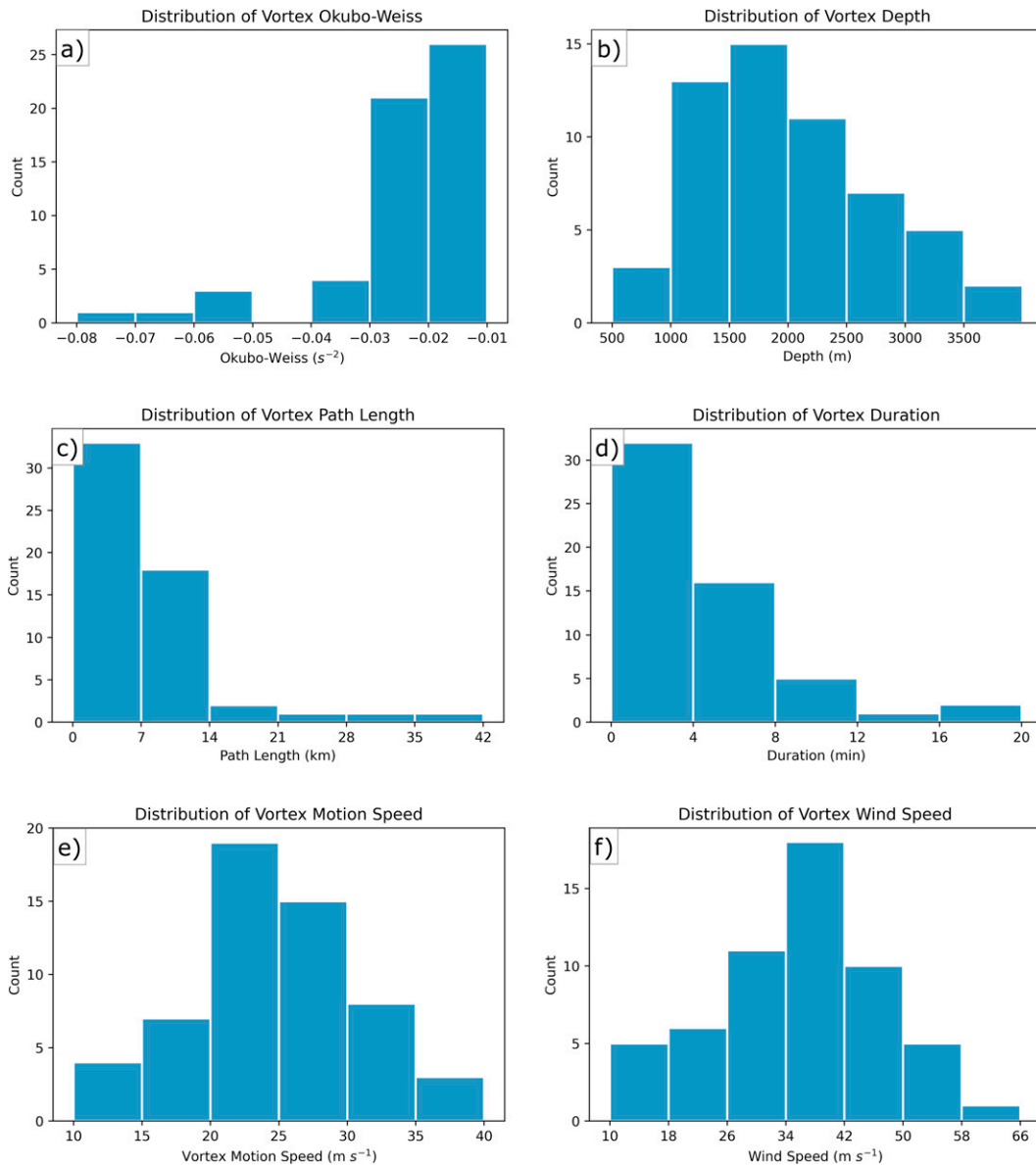
FIG. 6. Histogram plots for peak vortex intensity using (a) Okubo–Weiss, (b) peak vortex depth, (c) vortex path-length, (d) vortex duration, (e) average vortex motion, and (f) peak vortex near-surface wind speed for the 56 vortex tracks in the 200-m domains.

average duration (10.4 versus 3.9 min). The most intense vortices were also associated with 55% stronger average near-surface wind speeds (53.1 versus 34.2 m s^{-1}). Thus, the highest impact vortices would generally be the most detectable.

Because OW for pure vortices is the negative of the relative vertical vorticity squared, the sign of vorticity is masked in our approach. Thus, some of the objectively identified vortices could theoretically be anticyclonic. Prior numerical modeling studies (e.g., Trapp and Weisman 2003; Atkins and Laurent 2009b) have suggested that cyclonic–anticyclonic vortex couplets are common features of QLCSs. However, all of the 309 vortex points in the present simulation are cyclonic. Even when using a lower OW threshold of -0.0025 s^{-2}, there is

little to no evidence of cyclonic–anticyclonic couplets. Anti-cyclonic vortices represent only about 0.2% of vortices when using this lower threshold. Thus, vortex-genesis mechanisms that rely on the tilting of crosswise horizontal vorticity (Trapp and Weisman 2003; Wakimoto et al. 2006; Atkins et al. 2004) may not be predominant in this simulation.

b. Reflectivity signatures and kinematic structures

In addition to the properties of the vortices themselves, their associated reflectivity signatures and environmental characteristics can provide insights into storm structures and dynamical processes. Past research has identified several reflectivity signatures regularly associated with low-level
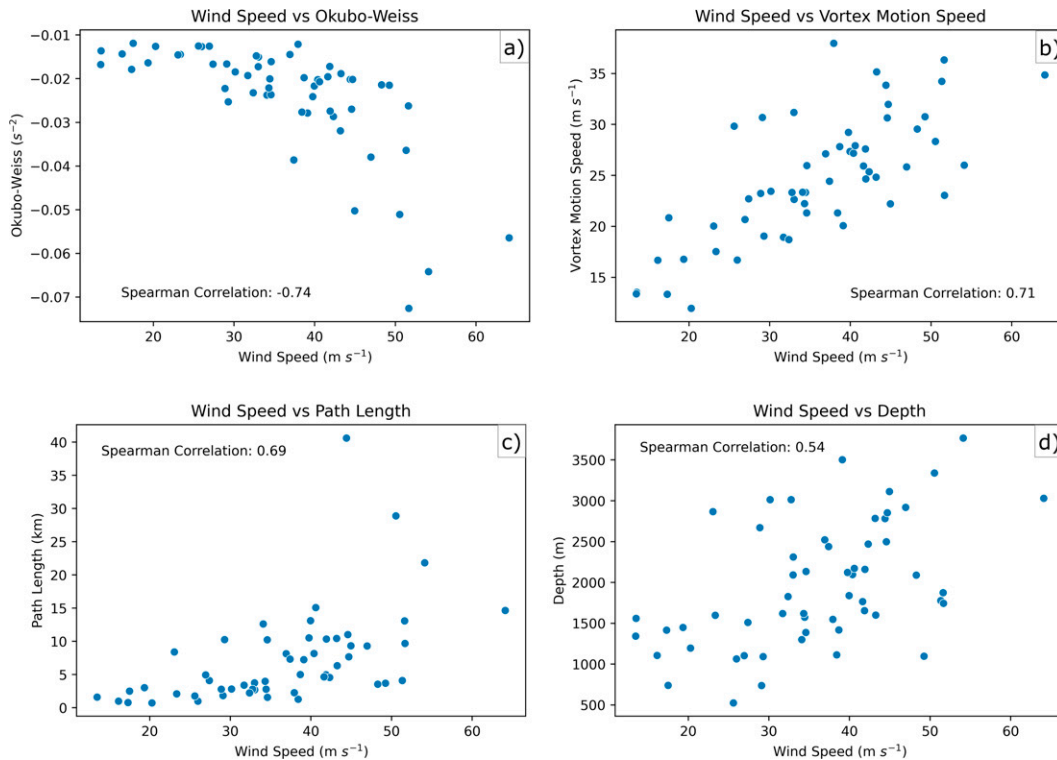
FIG. 7. Scatterplots of (a) surface wind speed and surface OW, (b) surface wind speed and vortex motion speed, (c) surface wind speed and pathlength, and (d) surface wind speed and vortex depth. Surface OW, surface wind speed, and vortex depth represent the maximum values along each vortex track. The Spearman correlation coefficient is provided in each plot. The sample size for each figure is 56.

rotation in HSLC QLCS events, including "broken-S" structures, embedded right-moving supercells, gust front cusps, and bow echoes (McAvoy et al. 2000; Grumm and Glazewski 2004; Lane and Moore 2006; Clark 2011; Smith et al. 2012; Davis and Parker 2014). Forecasters have also noted the utility of analyzing the low-level shear vector magnitude and orientation in operational settings (Lane and Moore 2006; Schaumann and Przybylinski 2012; Williams et al. 2018). Theory suggests that a near-balance of cold pool circulation and line-normal low-level vertical wind shear produces strong, upright updrafts (Rotunno et al. 1988), which could in turn stretch and amplify low-level vorticity to generate a surface vortex.

Throughout the event, the cold pools strengthen[5] and are robust enough to produce upshear tilt, so any increase in the line-normal component of the vertical wind shear would bolster the low-level updrafts. In the WRF simulation, vortices tend to be preferentially produced when the convective system is more nearly perpendicular to the low-level shear vector. The 0–3-km shear vectors in the pre-line environment remain virtually constant at approximately 25–30 m s^{-1} toward 45° azimuth (Fig. 8). The modeled parent QLCS has an overall orientation toward 45° (Fig. 4), but internal outflow

surges produce local bowing segments with more variable orientations. The local transition within the QLCS from a northeast–southwest toward a north–south orientation results in a substantial increase in the line-normal component of the 0–3-km shear vector from approximately 10–20 m s^{-1} between 2300 and 0200 UTC (Fig. 8). The role of these outflow surges increases over time, as evidenced by the cooler cold pools later in the system evolution. The cold pool evolution may partly explain the increased propensity for vortex production later in the QLCS's lifetime, with 21 vortices produced before 0000 UTC and 35 vortices produced after (Table 2). The localized zones of reorientation and subsequent vortex production lead to numerous cusps and small bowing segments, creating a line echo wave pattern in the simulated surface reflectivity later in the evolution (Figs. 8b,d).

Given the linkages between vortices and system structure, reflectivity signatures could aid in anticipating or detecting vortices. Unambiguous classification of reflectivity features is muddled by complex and rapid evolution, but three main reflectivity archetypes are documented in the WRF simulation, including gust front cusps/inflow notches, emerging convective line breaks (i.e., "broken-S"), and embedded supercell-like features. Interestingly, some vortices also form in areas of undifferentiated reflectivity. Although the reflectivity structures exhibit some similar features, the distinguishing characteristics of each are discussed in turn.

---

[5] Outflow winds increase from approximately 10–15 to 15–20 m s^{-1} (see Fig. S3 in the online supplemental material).
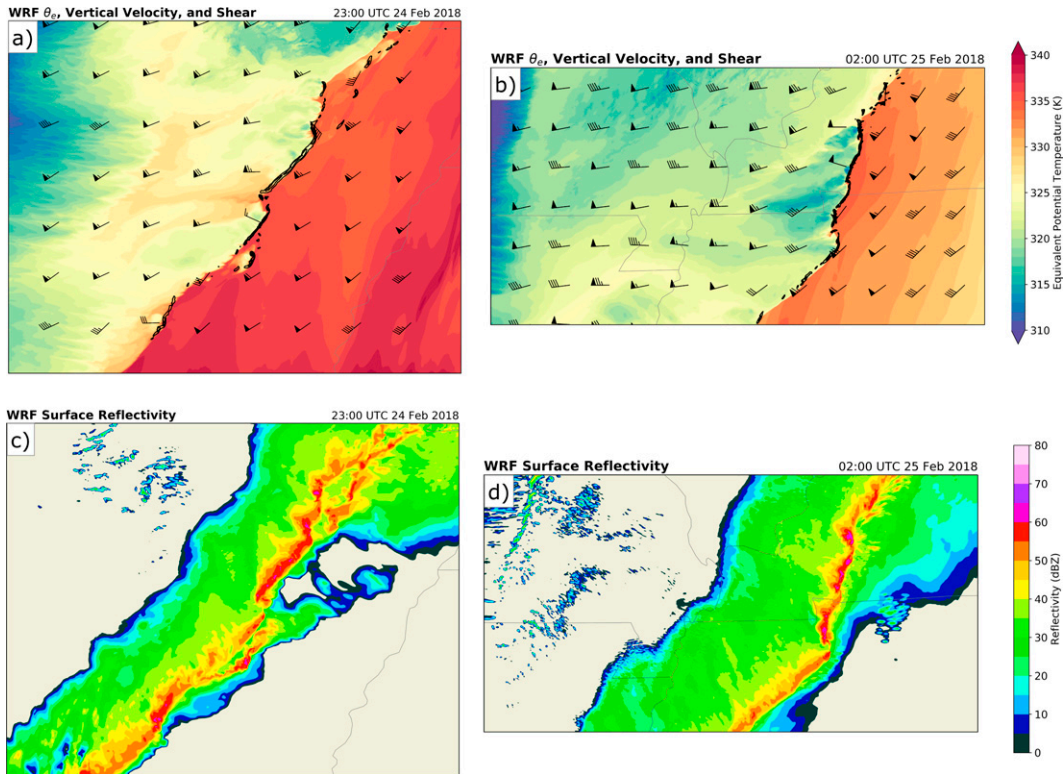
FIG. 8. Surface equivalent potential temperature (shaded; K), 3 km AGL vertical velocity (black contour; >10 m s^{-1}), and 0–3-km vertical wind shear (barbs; m s^{-1}) at (a) 2300 UTC 24 Feb 2018 (domain 3) and (b) 0200 UTC 25 Feb 2018 (domain 4). Surface reflectivity (shaded; dBZ) at (c) 2300 UTC 24 Feb 2018 (domain 3) and (d) 0200 UTC 25 Feb 2018 (domain 4).

Cusps or kinks along the gust front are associated with approximately 30%–35% of all surface vortices throughout the simulations. These cusps have horizontal length scales ranging from 1 to 6 km and bear some resemblance to those identified by Davis and Parker (2014). Most of these structures contain inflections or notches in the surface reflectivity near the inflow region (Figs. 9a,c). These structures are commonly associated with vortices in the bottom 40% of the intensity distribution, though a vortex in the 90th percentile is produced later in the simulation near a small bowing segment. Vortices that developed near smaller-scale gust front surges are also included in this class because they exhibit similar vertical structures. These vortices are primarily produced along the leading edge of the gust front ahead of a shield of precipitation several kilometers deep and near the most

substantial potential temperature gradients and coldest cold pools ($\Delta T = 6$–10 K; Figs. 9b,d).

Line breaks account for 15%–20% of the overall vortex population (e.g., Fig. 10). In the WRF simulation, such structures usually originate from differential gust front speeds across parts of the convective line, causing an "S" shape in the reflectivity field. In many cases, this line break precedes vortex development. However, on at least two occasions, this differential motion is the result (not the cause) of vortex-induced wind perturbations, with the "break" following vortex genesis. Regardless of how they came about, these structures are complex, evolve unpredictably (large variance in vortex duration), and produce low-level vortices that are quite intense (three such vortices have maximum near-surface wind speeds above 50 m s^{-1}).

Embedded supercell-like structures account for 30%–35% of vortices during the simulation. Examples of these structures in the horizontal plane are shown in Figs. 11a,c. Prior research suggests that embedded supercells may account for nearly 20% of all QLCS tornadoes as well as extensive damage (Schoen and Ashley 2011). The fraction of embedded supercell-like features may be higher throughout this event due to the strong deep-layer shear (30–40 m s^{-1}) in the environment, driving more hybrid-like storm modes. At least three strong (OW < -0.0225 s^{-2}) surface vortices are produced with these highly organized convective structures in

TABLE 2. Comparison of WRF simulated cold pool potential temperature deficits (K) in the core of the system cold pool and the number of simulated vortices throughout the early (2100–2359 UTC) and late (0000–0259 UTC) periods.

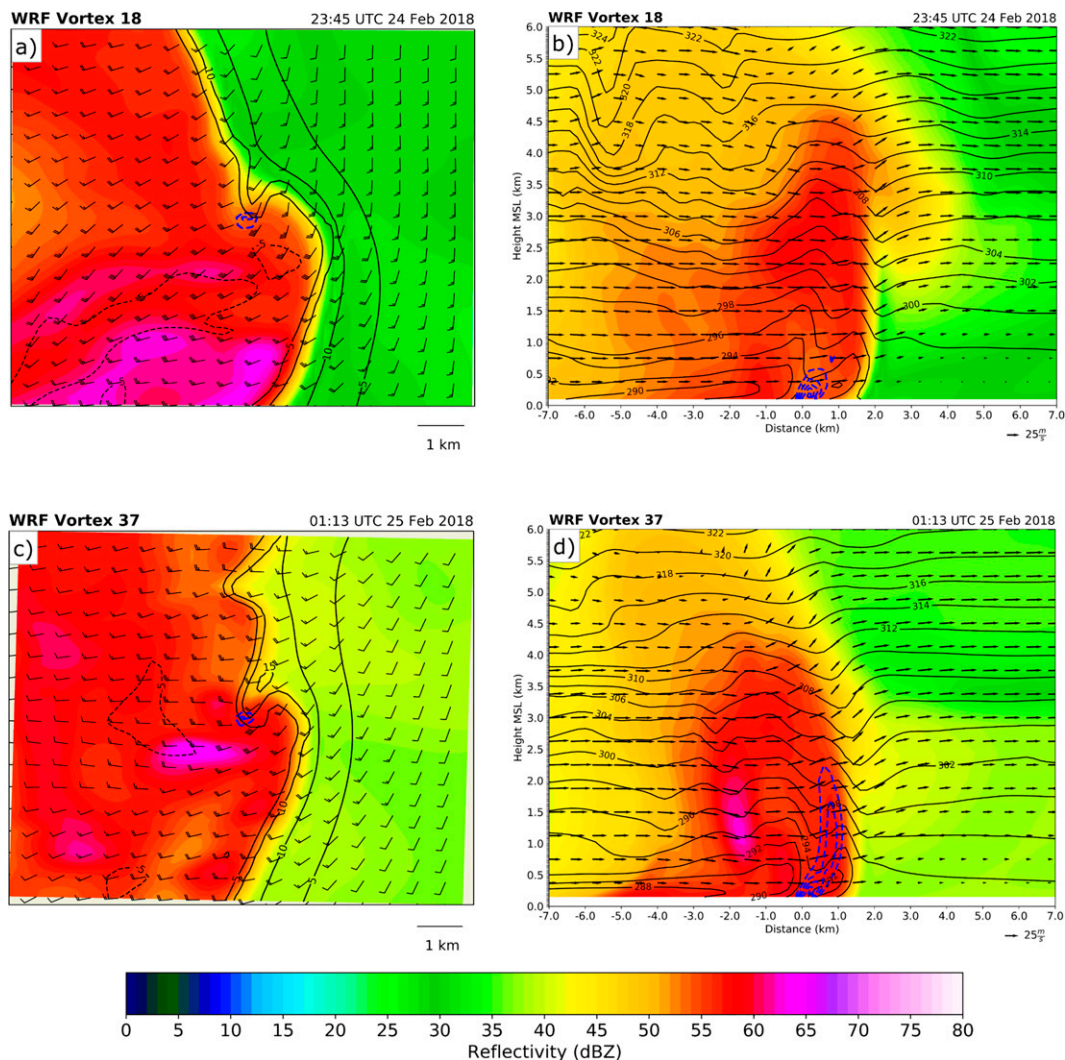| Time (UTC)	Avg potential temperature deficit (K)	No. of vortices
2100–2359	5.5	21
0000–0259	8.0	35

FIG. 9. Examples of gust front cusp and miniature bow echo structures. (a),(c) Plotted in horizontal plan view plots are surface reflectivity (shading; dBZ), surface Okubo–Weiss (blue contours; <-0.005 s^{-2}), surface ground-relative winds (barbs; m s^{-1}), and 1 km AGL vertical velocity (black contours; m s^{-1}). Barbs plotted every third grid point. Each plot is feature-centered at genesis time ($0.1° \times 0.1°$ area). (b),(d) Plotted in vertical cross-section plots are reflectivity (shading; dBZ), Okubo–Weiss (blue contours; <-0.0025 s^{-2}), ground-relative winds (vectors; m s^{-1}), and potential temperature (black contours; K). The orientation of each cross section is in the direction of vortex tilt (west–east for vortices 18 and 37).

the WRF simulation. Vertical cross sections through these events often reveal robust low- to midlevel mesocyclones and vigorous low-level updrafts (Figs. 11b,d). These intense, localized low-level updrafts below the level of free convection are most likely driven by dynamic lifting from vertical perturbation pressure gradient accelerations, as has been shown in supercell research (Klemp and Rotunno 1983; Klemp 1987). In some instances, the updrafts extend through 3–5 km AGL and exceed 30 m s^{-1}. Weak echo or bounded weak echo regions (BWER) are also common with the supercell-like structures as a result of intense low-level updrafts capable of rapidly advecting hydrometeors away vertically (Figs. 11b,d).

Surprisingly, vortices that form in areas of undifferentiated reflectivity account for 15%–20% of the vortices throughout the simulations. These signatures are most common between 2100 and 0100 UTC when the convection is generally less organized. Even in the absence of a strong reflectivity gradient, these vortices almost always form along a surface potential temperature gradient (see Fig. S4), indicative of a baroclinic zone with considerable convergence and horizontal vorticity. In general, once such a vortex develops, the corresponding flow field draws hydrometeors around the southern periphery, creating a hook-like structure. This feature usually develops 1–3 min after genesis. Vertical cross sections through these vortices reveal unimpressive or nonexistent midlevel
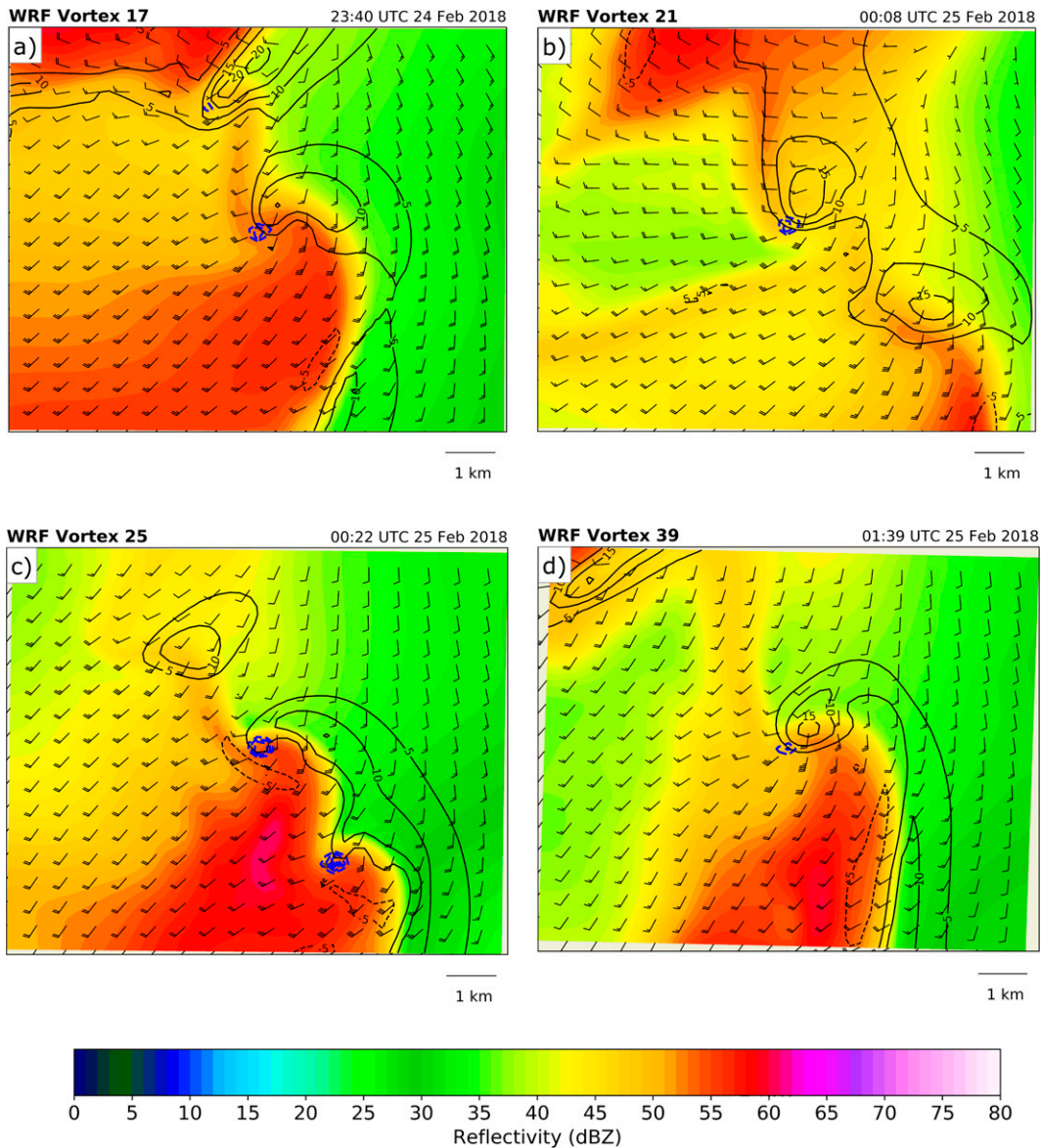
FIG. 10. Examples of convective line break structures as in Figs. 9a and 9c. Each plot is feature centered at genesis time ($0.1° \times 0.1°$ area).

updrafts yet ample near-ground vertical vorticity (not shown). Intense vortex production is possible when the low-level vorticity encounters a robust low- to midlevel updraft soon after genesis.

At least one strong vortex is associated with each of the reflectivity archetypes. Despite the many differences among the population of vortices, the updraft location is consistent among nearly all events with surface rotation located within a horizontal gradient in 1 km AGL vertical velocities with the updraft core invariably situated toward the north or northeast (i.e., Figs. 9–11). When updraft tilt and vortex tilt coincide (i.e., are in the same direction), vigorous stretching of the low-level vortex is most likely to occur. Occasionally, a corresponding downdraft exists south of the vortex, though this arrangement is most common among the supercell-like events where a structure resembling a rear-flank downdraft is present.

The null event reflectivity structures are remarkably similar to those from the stronger vortices (Fig. 12). However, vertical cross sections through the null events reveal some common updraft and vorticity structures that differ substantially from those in the strong vortex subset. Many null events have concentrated midlevel vertical vorticity coincident with strong midlevel updrafts but lack surface vorticity (Fig. 13a). Others that do have low-level vorticity lack a robust low-level updraft (i.e., >15 m s^{-1}) to induce ample stretching and surface vortex formation (Fig. 13b). About 15% of the null events do have coinciding low-level vertical vorticity and robust low-level updrafts very briefly, i.e., for 1–2 min (Fig. 13c). We
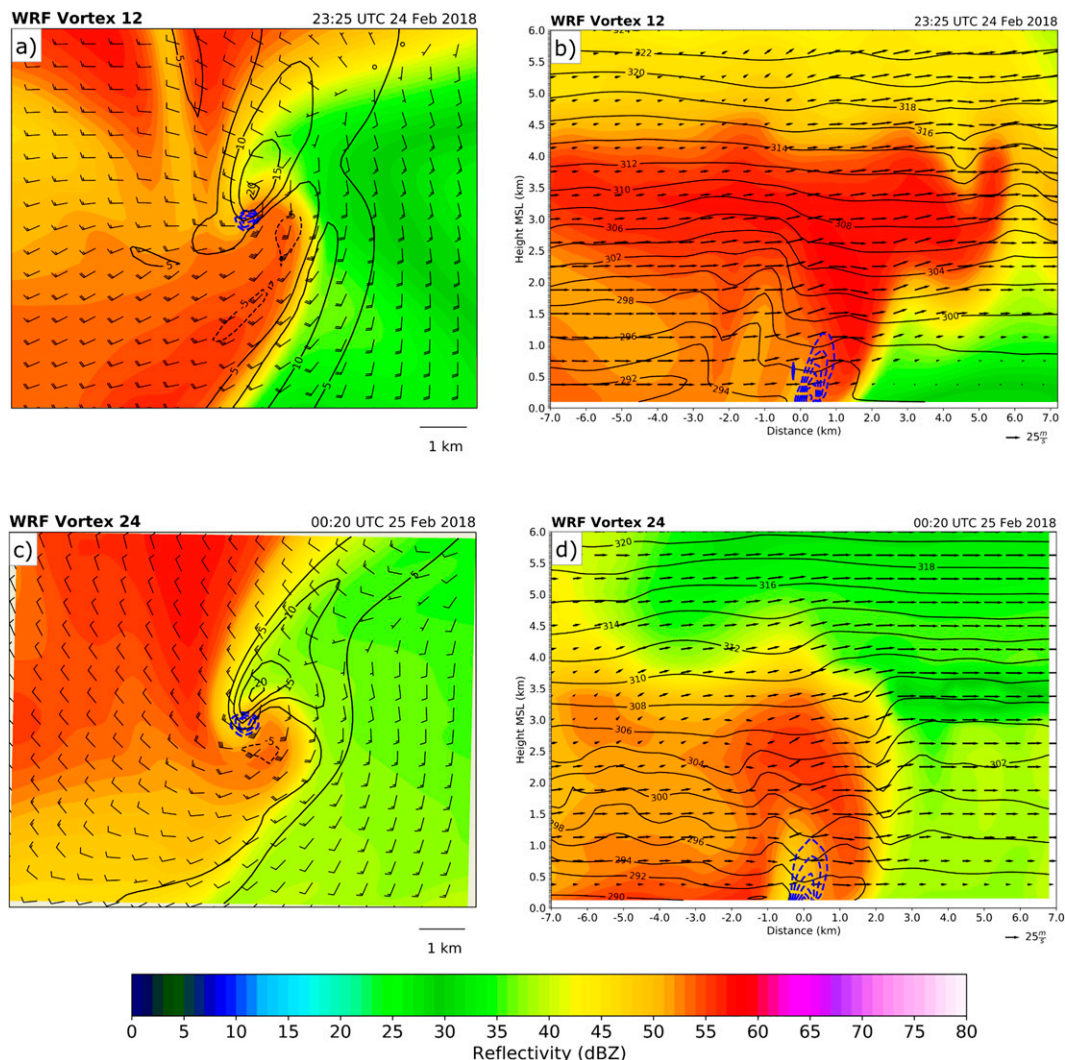
FIG. 11. Examples of embedded supercell-like structures as in Figs. 9a–d. The orientation of each cross section is in the direction of vortex tilt (west-southwest–east-northeast for vortex 12, northwest–southeast for vortex 24).

hypothesize that, in these cases, the process of tilting and stretching is too fleeting, such that there may not be enough time to generate a tornadic surface vortex (which may require several minutes). In general, the gust front updraft is significantly weaker in the first half of the simulation when fewer vortices are produced, possibly extending the time needed for sufficient vortex stretching.

While many of the weak (null) vortices have robust midlevel vorticity and midlevel updrafts (Fig. 14a), the most common trait among the strongest vortices is the persistent overlap of a vigorous low-level updraft and strong low-level vertical vorticity (Fig. 14b). This superposition often results in extreme stretching and amplification of surface vortices, analogous to the processes within tornadic supercells (Coffer and Parker 2017; Guarriello et al. 2018; Brown and Nowotarski 2019; Homeyer et al. 2020). Although the vertical structures are typically distinct between tornadic and nontornadic events, radar observations above ~1 km AGL may not distinguish them. For example, the 2 km

AGL relative vertical vorticity and updraft values adjacent to the OW feature are nearly identical in the null (Fig. 14a) and strong vortex (Fig. 14b) examples.

In terms of detection and warning, it is encouraging that the strongest vortices tend to be the deepest and longest-tracked. However, this population of vortices suggests that warning operations may continue to be challenging because many strong vortices are similar to null events above 1 km AGL, where radar sampling is robust. In response to this somewhat disappointing result, we next use these populations of simulated vortices to assess the possible role of the pre-line environment on vortex intensity.

4. Pre-storm environments

Near-inflow proximity soundings of the vortex and null events provide an opportunity to assess whether differences in surface vortex production can be linked to distinct environmental
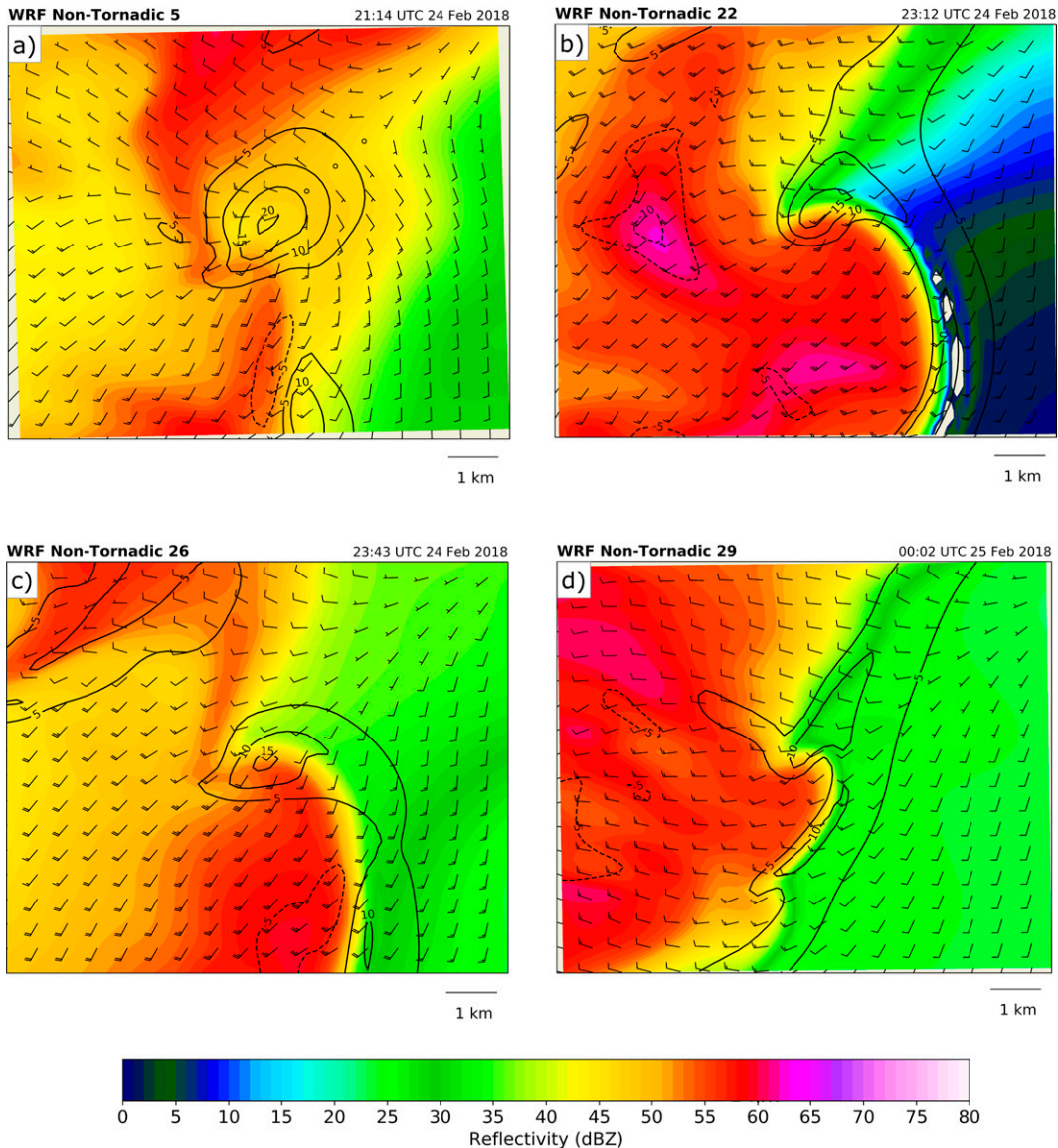
FIG. 12. Examples of objectively identified null events in domain 3 as in Fig. 12a and 12c. Each plot is feature centered at genesis time (0.1° × 0.1° area).

ingredients. Such a finding may be valuable in operational settings and shed light on key QLCS–environment interactions. Each vortex profile represents the near-inflow environment at the time of vortex genesis (i.e., the first occurrence of OW < -0.01 s^{-2}). To reduce the effects of sub-mesoscale fluctuations upon the point soundings, we obtain area-averaged profiles (5 km × 5 km) 40 km southeast (133° azimuth) of the vortex.[6] For each null event, vertical profiles are obtained near the inception of a sub-tornadic center of vorticity (i.e., when OW < -0.0025 s^{-2}) at or above the surface. Finescale terrain is also smoothed out by the areal averaging, and

larger-scale elevation gradients are small enough that the composite profile elevations are within 50 m.

One of the most intriguing aspects of the observed QLCS was the contrast between its earlier nontornadic period and its later tornadic period. Therefore, we focus only on the earlier null events in southern Arkansas (a cluster of more than 30 unsuccessful vortex-genesis events). Many of the null events later in the QLCS evolution occur near vortex events. When nontornadic events occur near tornadic events, the failure mechanism may result from a process internal to the convection or stochastic behavior (rather than the environment itself). Critical pre-QLCS environmental evolution can also occur on extremely small spatiotemporal scales (King et al. 2017), and poorly resolved heterogeneities may influence vortex development or intensity as well (e.g., mesoscale

---

[6] Two profiles are obtained from 40 km east-southeast (101° azimuth) because of proximity to the southern boundary of domain 4.
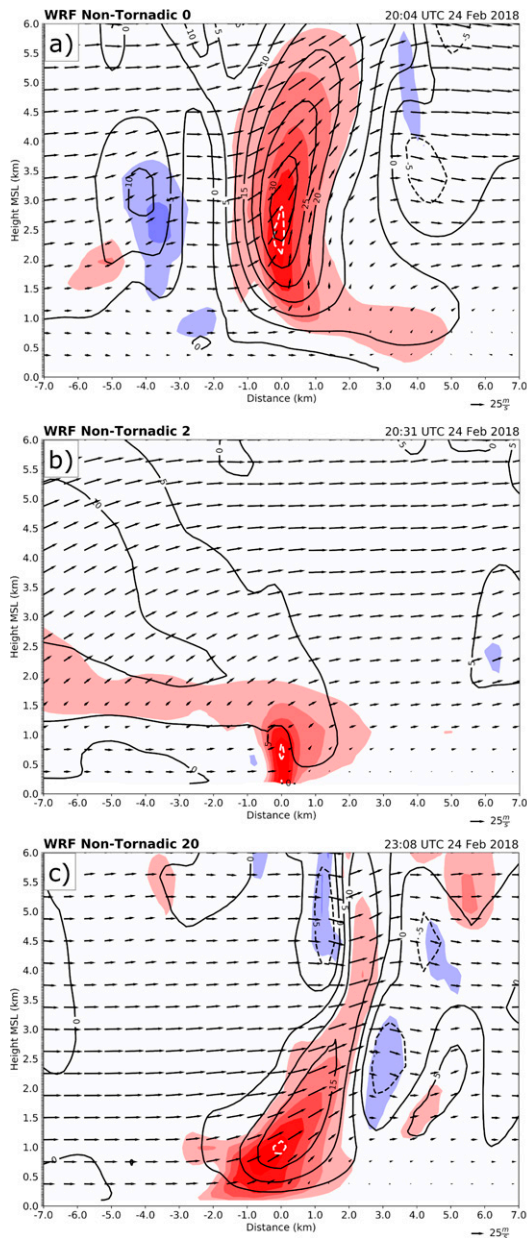
FIG. 13. Vertical cross sections through null event types including (a) midlevel vertical velocity and vorticity, (b) only low-level vertical vorticity, and (c) low-level vertical velocity and vorticity. Plotted are vertical vorticity (shading; s^{-1}), Okubo–Weiss (white contours; $< -0.0025 \, s^{-2}$), ground-relative winds (vectors; m s^{-1}), and vertical velocity (black contours; m s^{-1}). The orientation of all cross sections is southwest–northeast.

FIG. 14. Vertical structure of (a) a "typical" null event and (b) a "typical" strong vortex event as in Fig. 13. The orientation of the null cross section is southwest–northeast while the tornadic cross section is west-southwest–east-northeast.

boundaries, as discussed by Wheatley and Trapp 2008; Lyza et al. 2017; Coleman et al. 2018).

The composite vertical profiles (Fig. 15) from the null and vortex periods are similar. Both profiles have sufficient shear and instability to support severe convection. The wind profiles are almost indistinguishable in the low levels, with the vortex hodogra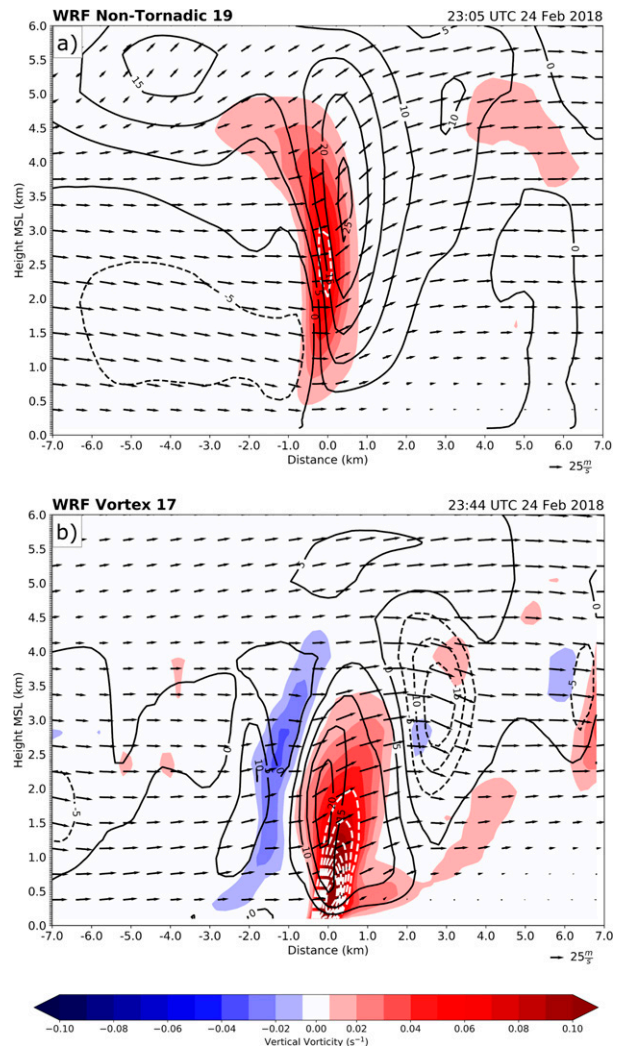ph being slightly longer due to stronger mid- to upper-level flow. Even though the amount of surface-based CAPE (SBCAPE) in both composites is similar, the null profile possesses taller, skinnier CAPE, with weak positive buoyancy through a deeper layer. The vortex profile possesses shorter, fatter CAPE, with larger positive buoyancy through a shallower layer. As suggested by the steeper low-level lapse rates, the lowering of the equilibrium level (EL) by 2 km in the tornadic subset indicates the potential for stronger vertical accelerations concentrated in the low levels. Similarly, Hochstatter (2021) noted the transition from pre-tornadic to tornadic phases of HSLC events is often marked by a reduction of the equilibrium level.

Although the composite soundings are similar, statistically significant differences exist between the distributions of several parameters. Of the parameters investigated, the most skillful in distinguishing between vortex and null events are
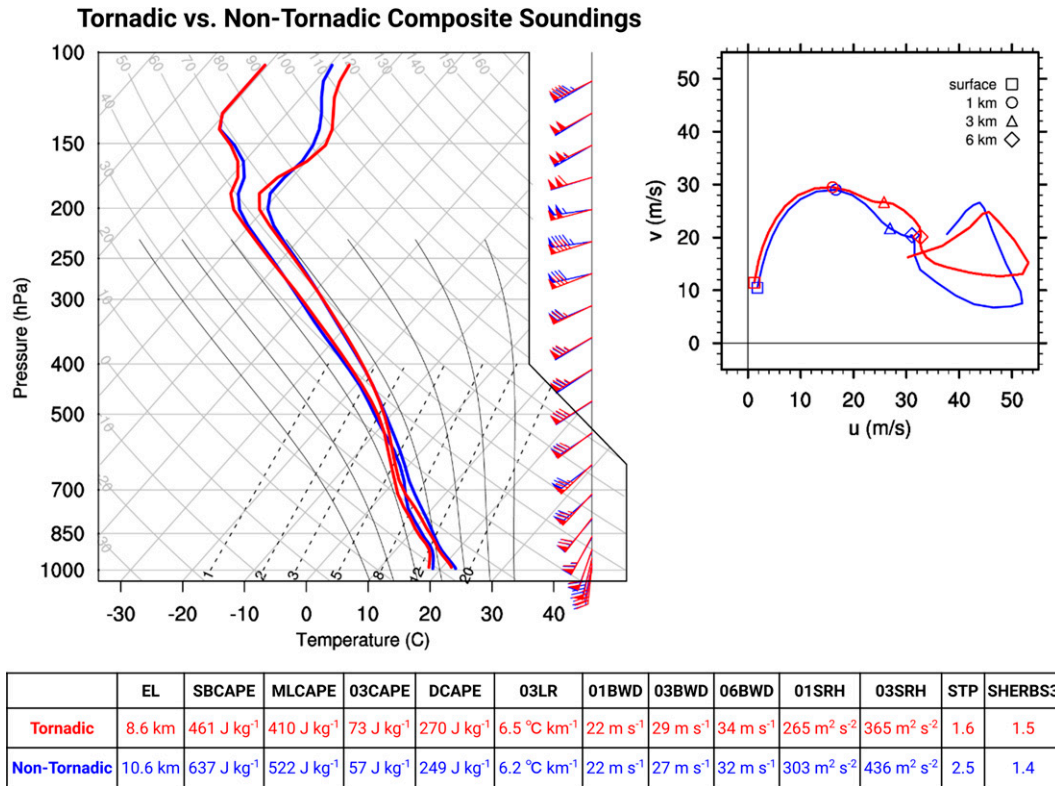
Tornadic vs. Non-Tornadic Composite Soundings

	EL	SBCAPE	MLCAPE	03CAPE	DCAPE	03LR	01BWD	03BWD	06BWD	01SRH	03SRH	STP	SHERBS3
Tornadic	8.6 km	461 J kg^{-1}	410 J kg^{-1}	73 J kg^{-1}	270 J kg^{-1}	6.5 °C km^{-1}	22 m s^{-1}	29 m s^{-1}	34 m s^{-1}	265 m^2 s^{-2}	365 m^2 s^{-2}	1.6	1.5
Non-Tornadic	10.6 km	637 J kg^{-1}	522 J kg^{-1}	57 J kg^{-1}	249 J kg^{-1}	6.2 °C km^{-1}	22 m s^{-1}	27 m s^{-1}	32 m s^{-1}	303 m^2 s^{-2}	436 m^2 s^{-2}	2.5	1.4

FIG. 15. Tornadic (red) and nontornadic (blue) composite vertical profiles and hodographs from areal-averaged (0.045° × 0.045°) near-inflow soundings from 40 km southeast of each event. Tornadic profile represents a composite of 56 soundings. Nontornadic profile represents a composite of 31 soundings. Sounding parameters include EL, SBCAPE, MLCAPE, 0–3-km CAPE (03CAPE), DCAPE, 0–1-km bulk wind difference (01BWD), 0–3-km BWD (03BWD), 0–6-km BWD (06BWD), 0–1-km SRH (01SRH), 0–3-km SRH (03SRH), STP, and SHERBS3. SRH values calculated using Bunkers right mover (RM) storm motions.

the 0–3-km lapse rates (Fig. 16c; $p < 0.0001$ from Welch's t test) and 0–6-km bulk wind difference (Fig. 16i; $p = 0.0025$ from Welch's t test). Among the vortex subset (i.e., all 56 vortices), vortex depth and surface wind speeds are also best correlated with 0–6-km shear magnitude ($r = 0.41$ and 0.45, respectively). Prior research supports the importance of these environmental proxies in distinguishing between non-severe and severe convective HSLC environments (Godfrey et al. 2004; Thompson et al. 2012). In addition, Sherburn and Parker (2014) and Sherburn et al. (2016) documented similar discriminatory skill for low-level lapse rates and shear vector magnitudes in HSLC environments. While steep low-level (0–3 km AGL) lapse rates appear to contribute to stronger low-level updrafts, strong low-level vertical wind shear tends to generate low-level vertical vorticity and produce more intense, upright updrafts when in the presence of an established cold pool (as in Sherburn and Parker 2019). Strong deep-layer shear also likely leads to more embedded supercell-like structures within a QLCS, consistent with the climatology from Smith et al. (2012). These embedded supercell-like structures are most often associated with longer-track mesocyclones and more intense surface vortices, as in this study and Atkins et al. (2004). Although the QLCS spans the early evening transition (EET), the low-level shear magnitudes uncharacteristically remain the same while

the deep-layer shear magnitudes increase across the EET. The relatively steady low-level shear may simply reflect the predominant role of the strongly forced synoptic environment.

Unfortunately, even though statistically significant differences exist between null and vortex environments within this event, the differences may not be practically meaningful to forecasters. For example, the difference in the 0–3-km lapse rates of 0.4 K km^{-1} and 0–6-km shear magnitudes of 2 m s^{-1} constitute about 5% of their total values and would typically fall within the same contour interval on coarsely gridded, smoothed operational mesoanalysis plots. Such a result generally confirms the visual similarities between the skew T–log$p$ and hodograph plots (cf. Fig. 15).

Two composite parameters,[7] the SHERBS3 and STP, are also examined for statistical significance in discriminating

---

[7] The significant hazards in environments with reduced buoyancy (SHERBS3) parameter using the 0–3-km shear magnitude (Sherburn and Parker 2014) multiplies the environmental 0–3-km shear, the 0–3-km lapse rate, and the 700–500-hPa lapse rate. The significant tornado parameter (STP; Thompson et al. 2012) multiplies the environmental CAPE, effective vertical wind shear, effective storm-relative helicity, and a measure of the height of the lifting condensation level (LCL).
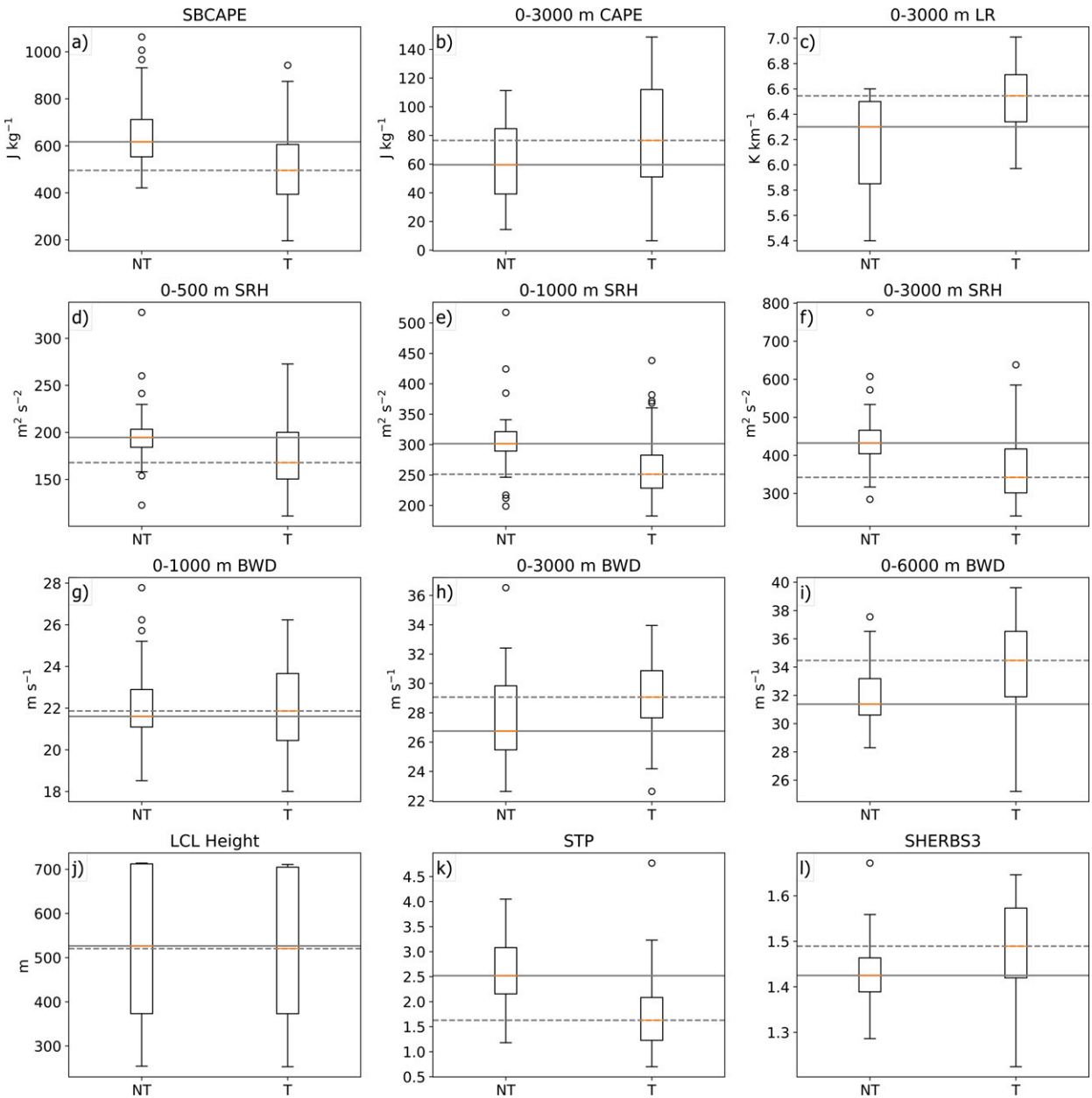
FIG. 16. Box-and-whisker plots of (a) SBCAPE, (b) 0–3000-m CAPE, (c) 0–3000-m lapse rate (LR), (d) 0–500-m SRH, (e) 0–1000-m SRH, (f) 0–3000-m SRH, (g) 0–3000-m BWD, (h) 0–3000-m BWD, (i) 0–6000-m BWD, (j) LCL height, (k) STP, and (l) SHERBS3 for the null (NT) and vortex (T) subsets of events. The solid line represents the median value of the null (NT) subset of 31 events. The dashed line represents the median value of the vortex (T) subset of 56 events.

between null and vortex events (Figs. 16k–l). In the present study, the mean SHERBS3 value for the vortex subset is statistically different from the null mean ($p = 0.0023$), though both values exceed the parameter's designated threshold of 1. The result from the STP comparison is also statistically significant ($p = 0.0058$), but the null subset has a higher STP value. Thus, STP has negative skill in discriminating between these subsets of events, primarily driven by the negative skill from SBCAPE (Fig. 16a). Brown et al. (2021)

similarly noted the limited utility of most common composite metrics in distinguishing between nontornadic and tornadic HSLC QLCS events. Coffer et al. (2019) also found CAPE to be, on average, higher in nontornadic supercell thunderstorms. Other moisture variables like precipitable water and dewpoint temperature are also larger in the nontornadic subset, while mixed-layer convective inhibition is identical between the two subsets. While downdraft CAPE (DCAPE) is higher in the tornadic subset, the values in

both subsets are low, and the differences are not statistically significant ($p = 0.2760$).

Storm-relative helicity (SRH) may generally be associated with vortex production in HSLC QLCS environments (see Table 4 of Anderson-Frey et al. 2019). Interestingly, for this event, SRH is not correlated with vortex production for any calculated depth (e.g., 0–250, 0–500, 0–1000, and 0–3000 m). In the context of typical values, the SRH in the pre-line environment is very high throughout both the null (nontornadic or NT) and vortex (tornadic or T) phases of the event (Figs. 16d–f). Nevertheless, SRH is not skillful in distinguishing which parts of the QLCS would produce strong vortices. Brown et al. (2021) also discovered the limited utility of SRH relative to thermodynamic variables in southeastern U.S. HSLC tornado environments.

Overall, despite the stark contrast in simulated vortex production, the early null (nontornadic) and later vortex (tornadic) pre-line environments are remarkably similar. Though the low-level lapse rate and deep-layer shear values are statistically different, the differences may not appear to be meaningful to a forecaster assessing the pre-storm environment. So, are these minute variations consequential enough to influence the dynamics of the convective system? Or, are they meteorologically insignificant (even if statistically significant)? We use the WRF composite profiles to initialize idealized simulations as a sensitivity test to address these questions.

5. Idealized simulations in pre-line environments

Idealized CM1 simulations help assess whether the marginal differences in WRF environmental profiles yield any meteorologically significant differences in basic storm properties. To account for differences in QLCS orientation that occur throughout the event, WRF composite profiles are rotated to preserve the boundary-relative components of the winds. Each of the WRF composite hodographs is used to produce two simulations, one assuming a line-oriented toward 45° azimuth (representing the southwest–northeast-oriented system) and the other a line-oriented toward 30° azimuth (representing the south-southwest–north-northeast-oriented segments). In total, we run four idealized simulations using the vortex (tornadic) event profile with 30° orientation (T30) or with 45° orientation (T45), and the null (nontornadic) event profile with 30° orientation (NT30) or with 45° orientation (NT45).

For both environmental profiles, the 30° line orientation (hodograph rotation) produces a robust convective system with leading (instead of trailing) stratiform precipitation, which results from the larger line-normal component of the deep-layer shear vector (Fig. 17). To a lesser degree, in both line orientations, the vortex (tornadic) base-state composite profile produces more robust QLCSs than the null (nontornadic) base-state counterparts (Fig. 17). Over the last hour of each CM1 simulation, the convective systems became progressively more cellular, with convective line breaks developing organically as a result of within-QLCS variability and vortex development (not shown). As in the WRF simulation, the flow fields associated with nascent embedded vortices

appear to contribute to the internal surges and convective line breaks. Embedded supercell-like structures with persistent, rotating updrafts are eventually present in each of the idealized simulations, implying that the age of the QLCS may also be relevant to the development of vortices, internal surges, and line segments with novel orientations (e.g., as in Sherburn and Parker 2019). Such a result may further explain why the observed and WRF simulated cases produce more frequent and more intense vortices over time.

We examine the vertical structure of the idealized convective systems by comparing 95th percentile values of reflectivity, updraft, and vertical vorticity (Fig. 18). The most intense convective systems are T30 and T45, with higher low- to midlevel vertical velocity and vertical vorticity. The weakest convective system appears to be NT45, with weaker low- to midlevel updrafts and surface reflectivity. System orientation has a leading-order influence on the shape of the vertical distribution with very similar vertical patterns in updraft and vorticity for these simulations (i.e., T30/NT30 and T45/NT45). Because both simulations with the "tornadic" profile are more robust than those initialized with the "nontornadic" profile, the thermodynamic and kinematic characteristics of the profile appear to have the most substantial influence on intensity, even as the overall system structures are more closely linked to the line orientation (Fig. 17).

The CM1 framework provides a baseline for convective evolution independent of large-scale lifting. The composite profiles, while similar, are sufficiently distinct to produce meteorologically meaningful differences in the simulations. While the convective mode is similar in each simulation, the ambient environment and system orientation modulate the severity and intensity of each QLCS. Discouragingly for forecasters, the minor thermodynamic and kinematic differences between the vortex (tornadic) and null (nontornadic) base-state profiles result in quantifiable differences among simulated convective systems in idealized environments. These signals suggest that the contrast in the WRF vortex production (i.e., early versus late) may be related to the subtle evolution of the pre-line environment. Such forecasting challenges may often be compounded by the rapid pre-line environment evolution in HSLC cases (King et al. 2017). In this study, we elected not to implement time-evolution of the CM1 environments in each run. Instead, because the CM1 simulations were intended to assess the behavior of each QLCS in the absence of large-scale evolution, we simulated the contrast between earlier (nontornadic) and later (tornadic) environments.

6. Conclusions

a. Summary

The HSLC QLCS from 24 to 25 February 2018 produced no tornadoes early in its lifespan and many tornadoes later on within a similar environment, making it quite pertinent to current operational challenges. This event exemplified a number of canonical HSLC QLCS attributes (e.g., shallow updrafts, modest cold pools), although more cases are needed in order to generalize these findings to other such cases (or to
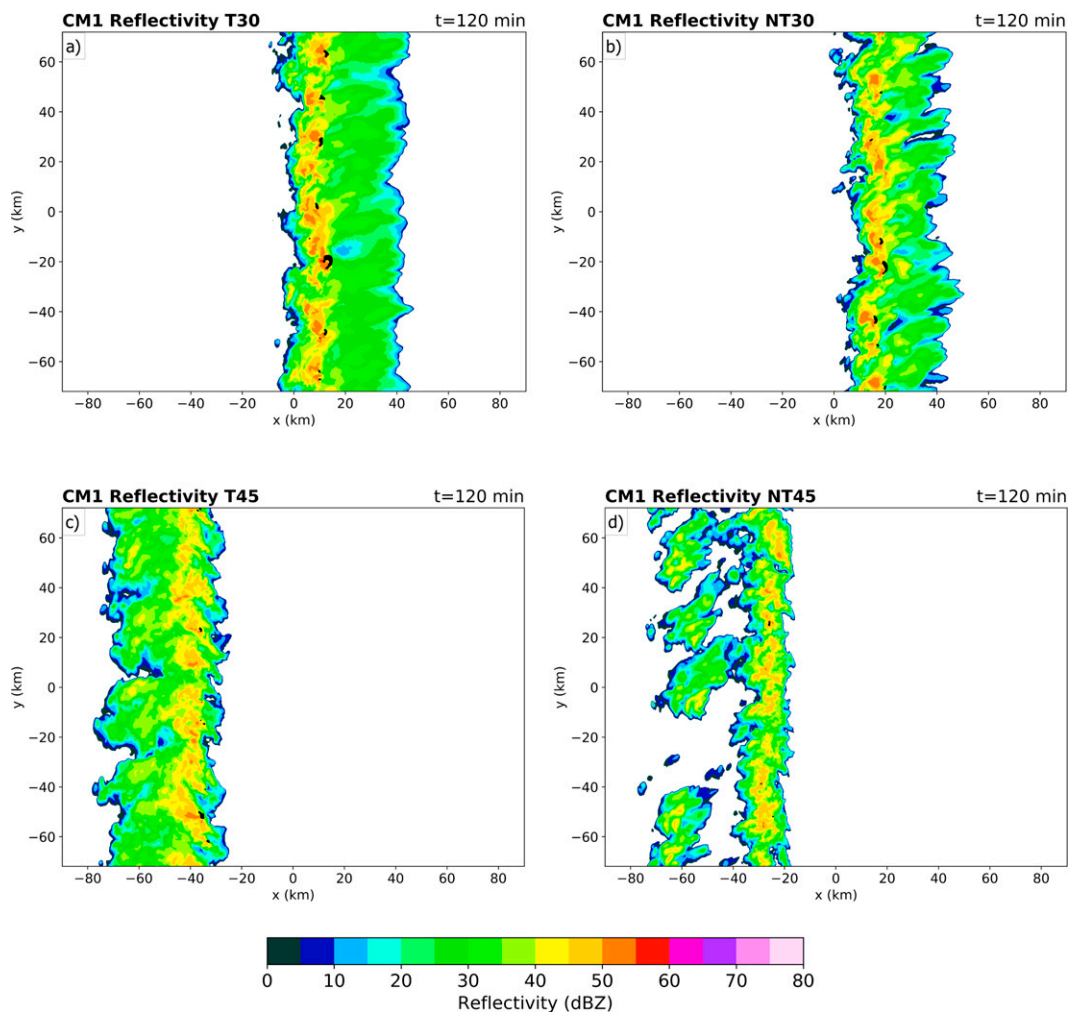
FIG. 17. CM1 surface reflectivity (shaded; dBZ) and 2–5-km updraft helicity (UH; contoured above 250 m^2 s^{-2}) at $t = 120$ min for (a) T30, (b) NT30, (c) T45, and (d) NT45.

recurring differences between QLCSs in high-CAPE versus low-CAPE environments).

A WRF simulation of the case captures the nontornadic period (early) and tornadic period (late) with distinct geographical distributions of simulated surface vortices. A population of 56 vortices is identified using an Okubo–Weiss threshold of -0.01 s^{-2} ($\zeta = 0.1$ s^{-1}). The median vortex has a maximum depth of 1803 m, a peak near-surface wind speed of 37.2 m s^{-1}, a duration of only 3 min, and a pathlength of only 4.6 km, implying substantial challenges for operational detection. In general, the stronger vortices tend to be deeper and longer-lived with more intense near-surface wind speeds than weaker vortices. The WRF simulation surprisingly lacks cyclonic–anticyclonic couplets, a finding that contrasts with past modeling studies (e.g., Trapp and Weisman 2003; Atkins and Laurent 2009b). Such a result may highlight the importance of ambient streamwise vorticity in QLCS environments.

Although more than 80% of the vortices are associated with gust front cusps/bow echoes, line breaks (i.e., "broken-S"),

and supercell-like structures, about 20% form in seemingly benign locations with no distinctive reflectivity structure. Vigorous near-surface updrafts (e.g., 30 m s^{-1}) below 1 km AGL characterize the most intense vortices. In stark contrast, the null events have midlevel rotation but lack near-ground vertical vorticity, low-level updrafts, or both. Approximately 20% of the null events briefly (i.e., for 1–2 min) have overlapping columns of low-level updraft and low-level vertical vorticity, reminiscent of the vertical structure in the tornadic events. In these cases, a surface vortex may have formed if the favorable conditions persisted for several more minutes (e.g., >3–5 min). Unfortunately for a forecaster, the reflectivity and velocity characteristics that best distinguish null and vortex structures are primarily confined to the lowest 1 km AGL, where radar coverage is often absent (especially at a distance).

Despite the differences in vortex production between the early (2100–2359 UTC) and late (0000–0259 UTC) periods, the environments are strikingly similar. The composite profile
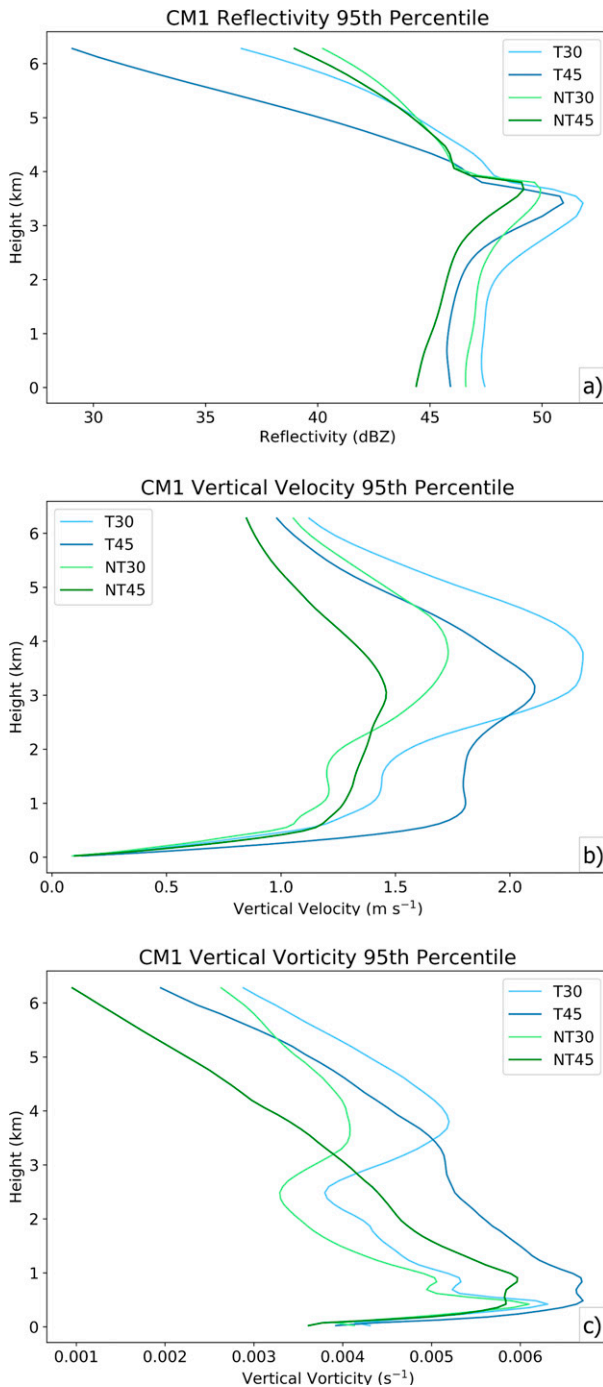
FIG. 18. 95th percentile value comparisons of (a) reflectivity, (b) updraft, and (c) vertical vorticity as a function of height. Percentiles calculated at each vertical level through 6 km AGL from 60 to 180 min in each simulation.

from each subset of events (i.e., vortices versus nulls) depicts favorable conditions for severe convection with strong vertical wind shear and marginal instability. The distributions of 0–3-km and 0–6-km vertical wind shear are statistically different, with a preference for more intense vortices in more strongly sheared

environments. While vortices do form when the low-level shear vector is largely parallel to the convective line, significant line-normal wind shear (associated with reorientation of segments within the QLCS) appears to be more favorable for low-level vortex formation. In addition, the distributions of 0–3-km lapse rate and 0–3-km CAPE are statistically different for the subsets. However, all of these statistical differences are small compared to the magnitudes of the fields themselves (typically <10%), so they may not be meaningful to a forecaster assessing tornado potential.

Even so, CM1 simulations initialized with each composite profile reveal that the small kinematic and thermodynamic differences are consequential for QLCS evolution and severity. The vortex (tornadic) profile produces a stronger overall QLCS with more robust updrafts and more low- to midlevel vertical vorticity. Additionally, when the shear vector is more line-perpendicular (30° rotation), more near-surface condensate, stronger midlevel updrafts, and greater midlevel vertical vorticity is observed.

b. Findings

The confirmatory findings from our simulations are as follows:

- Most surface vortices are short-lived and weak, but stronger vortices can occur.
- Strong vortices tend to be deeper and longer-lived with more intense near-surface wind speeds than weaker vortices. Vortex intensity, depth, and wind speeds were all well-correlated for the WRF simulated population of vortices.
- At least one strong vortex is associated with each reflectivity archetype analyzed herein (i.e., gust front cusp/bow echo, line break, supercell-like, etc.).

The more novel findings from our simulations are as follows:

- Intense vortices have a distinct vertical structure with robust columns of vertical vorticity and intense low-level updrafts.
- Composite profiles of null (nontornadic) and vortex (tornadic) environments are similar but have statistically significant differences in low-level lapse rates, low-level CAPE, low-level vertical wind shear, and deep-layer vertical wind shear.
- In idealized simulations, the minute thermodynamic and kinematic differences influence convective system intensity, with profile characteristics having the most substantial influence on system intensity while line orientation (relative to shear) affects overall system structure.

The present study reiterates the current limitations associated with QLCS surface vortex prediction and detection. Although precursor centers of vorticity may persist in the low- to midlevels, these features are not unique to the strong (i.e., likely tornadic) vortex events. The most distinctive characteristics of the strong vortices are low-level vorticity and a coinciding updraft near the surface (i.e., at or below 1 km AGL). When these surface vortices do form, they persist for at least 5 min (i.e., the average time for a full WSR-88D

volume scan) only 40% of the time. Even the subset of the most intense vortices (peak $\zeta = 0.2$ m s^{-1}) maintain requisite surface rotation for only about 10 min. Thus, both detection and forecasting of QLCS vortices in real-time may require spatial and temporal resolution that is not presently available.

c. Future work

Future work should examine other cases to understand the generality of our results. Given the small horizontal length scales of HSLC QLCS vortices, modeling studies with even finer grid spacing could further investigate the role of sub-convective-scale wind perturbations and sub-tornadic centers of vorticity on vortex intensification. Additionally, a focused analysis on an ensemble of idealized simulations with perturbed hodographs may be insightful for determining the degree to which stochasticity of storm-scale processes affects tornadogenesis. A radar emulator applied to high-resolution model output may help diagnose potential precursors leading up to vortex genesis. Observational studies with high spatial and temporal resolution would also be useful to validate modeling studies such as this. Finally, the preliminary analysis of vorticity origins in simulated HSLC QLCS vortices conducted by Lovell (2020) could be expanded to include a more thorough investigation of vorticity sources. Such analyses could also shed light on generation mechanisms and how these may vary across environments and storm types. The long-range goal of such work is to advance forecasting and warning operations both for QLCSs in general and within operationally demanding HSLC environments.

Data availability statement. The CM1 model code is available from https://www2.mmm.ucar.edu/people/bryan/cm1/. The WRF Model code is available from https://www2.mmm.ucar.edu/wrf/users/downloads.html. Other materials including source data, input files, and post-processing scripts are available from the author by request.

REFERENCES

Anderson-Frey, A., Y. Richardson, A. Dean, R. Thompson, and B. Smith, 2016: Investigation of near-storm environments for tornado events and warnings. *Wea. Forecasting*, **31**, 1771–1790, https://doi.org/10.1175/WAF-D-16-0046.1.

——, ——, ——, R. Thomspon, and B. Smith, 2019: Characteristics of tornado events and warnings in the southeastern United States. *Wea. Forecasting*, **34**, 1017–1034, https://doi.org/10.1175/WAF-D-18-0211.1.

Ashley, W., and S. Strader, 2016: Recipe for disaster: How the dynamic ingredients of risk and exposure are changing the tornado disaster landscape. *Bull. Amer. Meteor. Soc.*, **97**, 767–786, https://doi.org/10.1175/BAMS-D-15-00150.1.

Atkins, N., and M. S. Laurent, 2009a: Bow echo mesovortices. Part I: Processes that influence their damaging potential. *Mon. Wea. Rev.*, **137**, 1497–1513, https://doi.org/10.1175/2008MWR2649.1.

——, and ——, 2009b: Bow echo mesovortices. Part II: Their genesis. *Mon. Wea. Rev.*, **137**, 1514–1532, https://doi.org/10.1175/2008MWR2650.1.

——, J. Arnott, and R. Przybylinski, 2004: Vortex structure and evolution within bow echoes. Part I: Single-Doppler and damage analysis of the 29 June 1998 derecho. *Mon. Wea. Rev.*, **132**, 2224–2242, https://doi.org/10.1175/1520-0493(2004)132<2224:VSAEWB>2.0.CO;2.

Benjamin, S., G. Grell, J. Brown, T. Smirnova, and R. Bleck, 2004: Mesoscale weather prediction with the RUC hybrid isentropic–terrain-following coordinate model. *Mon. Wea. Rev.*, **132**, 473–494, https://doi.org/10.1175/1520-0493(2004)132<0473:MWPWTR>2.0.CO;2.

Bothwell, P., J. Hart, and R. Thompson, 2002: An integrated three-dimensional objective analysis scheme in use at the Storm Prediction Center. *21st Conf. on Severe Local Storms*, San Antonio, TX, Amer. Meteor. Soc., JP3. 1, https://ams.confex.com/ams/SLS_WAF_NWP/techprogram/paper_47482.htm.

Brown, M., and C. Nowotarski, 2019: The influence of lifting condensation level on low-level outflow and rotation in simulated supercell thunderstorms. *J. Atmos. Sci.*, **76**, 1349–1372, https://doi.org/10.1175/JAS-D-18-0216.1.

——, ——, A. Dean, B. Smith, R. Thompson, and J. Peters, 2021: The early evening transition in southeastern U.S. tornado environments. *Wea. Forecasting*, **36**, 1431–1452, https://doi.org/10.1175/WAF-D-20-0191.1.

Bryan, G., and M. Fritsch, 2002: A benchmark simulation for moist nonhydrostatic numerical models. *Mon. Wea. Rev.*, **130**, 2917–2928, https://doi.org/10.1175/1520-0493(2002)130<2917:ABSFMN>2.0.CO;2.

——, and H. Morrison, 2012: Sensitivity of a simulated squall line to horizontal resolution and parameterization of microphysics. *Mon. Wea. Rev.*, **140**, 202–225, https://doi.org/10.1175/MWR-D-11-00046.1.

Carbone, R., 1982: A severe frontal rainband. Part I. Stormwide hydrodynamic structure. *J. Atmos. Sci.*, **39**, 258–279, https://doi.org/10.1175/1520-0469(1982)039<0258:ASFRPI>2.0.CO;2.

Clark, M., 2011: Doppler radar observations of mesovortices within a cool-season tornadic squall line over the UK. *Atmos. Res.*, **100**, 749–764, https://doi.org/10.1016/j.atmosres.2010.09.007.

Coffer, B., and M. Parker, 2017: Simulated supercells in nontornadic and tornadic VORTEX2 environments. *Mon. Wea. Rev.*, **145**, 149–180, https://doi.org/10.1175/MWR-D-16-0226.1.

——, ——, R. Thompson, B. Smith, and R. Jewell, 2019: Using near-ground storm relative helicity in supercell tornado forecasting. *Wea. Forecasting*, **34**, 1417–1435, https://doi.org/10.1175/WAF-D-19-0115.1.

Cohen, A., S. Cavallo, M. Coniglio, H. Brooks, and I. Jirak, 2017: Evaluation of multiple planetary boundary layer parameterization schemes in southeast U.S. cold season severe thunderstorm environments. *Wea. Forecasting*, **32**, 1857–1884, https://doi.org/10.1175/WAF-D-16-0193.1.

Coleman, T., A. Lyza, K. Knupp, K. Laws, and W. Wyatt, 2018: A significant tornado in a heterogeneous environment during VORTEX-SE. *Electron. J. Severe Storms Meteor.*, **13** (2), https://ejssm.org/archives/2018/vol-13-2-2018/.

Conrad, D., and K. Knupp, 2019: Doppler radar observations of horizontal shearing instability in quasi-linear convective systems. *Mon. Wea. Rev.*, **147**, 1297–1318, https://doi.org/10.1175/MWR-D-18-0257.1.

Davis, J., and M. Parker, 2014: Radar climatology of tornadic and nontornadic vortices in high shear, low-CAPE environments in the mid-Atlantic and southeastern United States. *Wea. Forecasting*, **29**, 828–853, https://doi.org/10.1175/WAF-D-13-00127.1.

Dean, A., and R. Schneider, 2008: Forecast challenges at the NWS Storm Prediction Center relating to the frequency of favorable severe storm environments. *24th Conf. on Severe Local Storms*, Savannah, GA, Amer. Meteor. Soc., 9A.2, https://ams.confex.com/ams/24SLS/techprogram/paper_141743.htm.

Dudhia, J., 2014: Overview of WRF physics. NCAR, 102 pp., http://homepages.see.leeds.ac.uk/~lecag/wiser/sample_wiser_files.dir/Physics_Dudhia.ppt.pdf.

Flournoy, M., and M. Coniglio, 2019: Origins of vorticity in a simulated tornadic mesovortex observed during PECAN on 6 July 2015. *Mon. Wea. Rev.*, **147**, 107–134, https://doi.org/10.1175/MWR-D-18-0221.1.

Funk, T., K. Darmofal, J. Kirkpatrick, V. Dewald, R. Przybylinski, G. Schmocker, and Y.-J. Lin, 1999: Storm reflectivity and mesocyclone evolution associated with the 15 April 1994 squall line over Kentucky and southern Indiana. *Wea. Forecasting*, **14**, 976–993, https://doi.org/10.1175/1520-0434(1999)014<0976:SRAMEA>2.0.CO;2.

Godfrey, E., R. Trapp, and H. Brooks, 2004: A study of the prestorm environment of tornadic quasi-linear convective systems. *22nd Conf. on Severe Local Storms*, Hyannis, MA, Amer. Meteor. Soc., 3A.5, https://ams.confex.com/ams/11aram22sls/techprogram/paper_81388.htm.

Grumm, R., and M. Glazewski, 2004: Thunderstorm types associated with the "broken-S" radar signature. *22nd Conf. on Severe Local Storms*, Hyannis, MA, Amer. Meteor. Soc., P7.1, https://ams.confex.com/ams/11aram22sls/webprogram/Paper81537.html.

Guarriello, F., C. Nowotarski, and C. Epifanio, 2018: Effects of the low-level wind profile on outflow position and near-surface vertical vorticity in simulated supercell thunderstorms. *J. Atmos. Sci.*, **75**, 731–753, https://doi.org/10.1175/JAS-D-17-0174.1.

Hochstatter, L., 2021: Spatial and temporal variability of tornadic versus non-tornadic high-shear, low-CAPE environments. M.S. thesis, Department of Marine, Earth, and Atmospheric Sciences, University of North Carolina.

Homeyer, C., T. Sandmæl, C. Potvin, and A. Murphy, 2020: Distinguishing characteristics of tornadic and nontornadic supercell storms from composite mean analyses of radar observations. *Mon. Wea. Rev.*, **148**, 5015–5040, https://doi.org/10.1175/MWR-D-20-0136.1.

Iacono, M., J. Delamere, E. Mlawer, M. Shephard, S. Clough, and W. Collins, 2008: Radiative forcing by long-lived greenhouse gases: Calculations with the AER radiative transfer models. *J. Geophys. Res.*, **113**, D13103, https://doi.org/10.1029/2008JD009944.

King, J., M. Parker, K. Sherburn, and G. Lackmann, 2017: Rapid evolution of cool season, low-CAPE severe thunderstorm environments. *Wea. Forecasting*, **32**, 763–779, https://doi.org/10.1175/WAF-D-16-0141.1.

Klemp, J., 1987: Dynamics of tornadic thunderstorms. *Annu. Rev. Fluid Mech.*, **19**, 369–402, https://doi.org/10.1146/annurev.fl.19.010187.002101.

——, and R. Rotunno, 1983: A study of the tornadic region within a supercell thunderstorm. *J. Atmos. Sci.*, **40**, 359–377, https://doi.org/10.1175/1520-0469(1983)040<0359:ASOTTR>2.0.CO;2.

Lane, J., and P. Moore, 2006: Observations of a non-supercell tornadic thunderstorm from a terminal Doppler weather radar. *23rd Conf. on Severe Local Storms*, St. Louis, MO, Amer. Meteor. Soc., 4.5, https://ams.confex.com/ams/23SLS/webprogram/Paper115102.html.

Lee, B., and R. Wilhelmson, 1997: The numerical simulation of non-supercell tornadogenesis. Part I: Initiation and evolution of pretornadic misocyclone circulations along a dry outflow boundary. *J. Atmos. Sci.*, **54**, 32–60, https://doi.org/10.1175/1520-0469(1997)054<0032:TNSONS>2.0.CO;2.

Lovell, L., 2020: Examining the structure and dynamics of QLCS vortices in high-shear, low-CAPE environments. M.S. thesis, Department of Marine, Earth, and Atmospheric Sciences, North Carolina State University.

Lyza, A., A. Clayton, K. Knupp, E. Lenning, M. Friedlein, R. Castro, and E. Bentley, 2017: Analysis of mesovortex characteristics, behavior, and interactions during the second 30 June–1 July 2014 Midwestern derecho event. *Electron. J. Severe Storms Meteor.*, **12** (2), https://ejssm.org/archives/2017/vol-12-2-2017/.

McAvoy, B., W. Jones, and P. Moore, 2000: Investigation of an unusual storm structure associated with weak to occasionally strong tornadoes over the eastern United States. *20th Conf. on Severe Local Storms*, Orlando, FL, Amer. Meteor. Soc., 6.5, https://ams.confex.com/ams/Sept2000/techprogram/paper_16490.htm.

Okubo, A., 1970: Horizontal dispersion of floatable particles in the vicinity of velocity singularities such as convergences. *Deep-Sea Res.*, **17**, 445–454, https://doi.org/10.1016/0011-7471(70)90059-8.

Parker, M., 2021: Self-organization and maintenance of simulated nocturnal convective systems from PECAN. *Mon. Wea. Rev.*, **149**, 999–1022, https://doi.org/10.1175/MWR-D-20-0263.1.

——, B. Borchardt, R. Miller, and C. Ziegler, 2020: Simulated evolution and severe wind production by the 25–26 June 2015 nocturnal MCS from PECAN. *Mon. Wea. Rev.*, **148**, 183–209, https://doi.org/10.1175/MWR-D-19-0072.1.

Przybylinski, R., 1995: The bow echo: Observations, numerical simulations, and severe weather detection methods. *Wea. Forecasting*, **10**, 203–218, https://doi.org/10.1175/1520-0434(1995)010<0203:TBEONS>2.0.CO;2.

Rotunno, R., J. Klemp, and M. Weisman, 1988: A theory for strong, long-lived squall lines. *J. Atmos. Sci.*, **45**, 463–485, https://doi.org/10.1175/1520-0469(1988)045<0463:ATFSLL>2.0.CO;2.

Schaumann, J., and R. Przybylinski, 2012: Operational application of 0-3 km bulk shear vectors in assessing Quasi Linear Convective System mesovortex and tornado potential. *26th Conf. on Severe Local Storms*, Nashville, TN, Amer. Meteor. Soc., 142, https://ams.confex.com/ams/26SLS/webprogram/Paper212008.html.

Schenkman, A., M. Xue, and A. Shapiro, 2012: Tornadogenesis in a simulated mesovortex within a mesoscale convective system. *J. Atmos. Sci.*, **69**, 3372–3390, https://doi.org/10.1175/JAS-D-12-038.1.

Schoen, J., and W. Ashley, 2011: A climatology of fatal convective wind events by storm type. *Wea. Forecasting*, **26**, 109–121, https://doi.org/10.1175/2010WAF2222428.1.

Sherburn, K., and M. Parker, 2014: Climatology and ingredients of significant severe convection in high-shear, low-CAPE environments. *Wea. Forecasting*, **29**, 854–877, https://doi.org/10.1175/WAF-D-13-00041.1.

——, and ——, 2019: The development of severe vortices within simulated high-shear, low-CAPE convection. *Mon. Wea. Rev.*, **147**, 2189–2216, https://doi.org/10.1175/MWR-D-18-0246.1.

——, ——, J. King, and G. Lackmann, 2016: Composite environments of severe and nonsevere high-shear, low-CAPE convective events. *Wea. Forecasting*, **31**, 1899–1927, https://doi.org/10.1175/WAF-D-16-0086.1.

Skamarock, W., and Coauthors, 2019: A description of the Advanced Research WRF Model version 4. NCAR Tech. Note NCAR/TN-556+STR, 145 pp., https://doi.org/10.5065/1dfh-6p97.

Smith, B., J. Guyer, and A. Dean, 2008: The climatology, convective mode, and mesoscale environment of cool season severe thunderstorms in the Ohio and Tennessee valleys, 1995–2006. *24th Conf. on Severe Local Storms*, Savannah, GA, Amer. Meteor. Soc., 13B.7, https://ams.confex.com/ams/24SLS/webprogram/Paper141968.html.

——, R. Thompson, J. Grams, C. Broyles, and H. Brooks, 2012: Convective modes for significant severe thunderstorms in the contiguous United States. Part I: Storm classification and climatology. *Wea. Forecasting*, **37**, 1114–1135, https://doi.org/10.1175/WAF-D-11-00115.1.

Strader, S., and W. Ashley, 2018: Finescale assessment of mobile home tornado vulnerability in the central and Southeast United States. *Wea. Climate Soc.*, **10**, 797–812, https://doi.org/10.1175/WCAS-D-18-0060.1.

Thompson, G., P. Field, R. Rasmussen, and W. Hall, 2008: Explicit forecasts of winter precipitation using an improved bulk microphysics scheme. Part II: Implementation of a new snow parameterization. *Mon. Wea. Rev.*, **136**, 5095–5115, https://doi.org/10.1175/2008MWR2387.1.

Thompson, R., B. Smith, J. Grams, A. Dean, and C. Broyles, 2012: Convective modes for significant severe thunderstorms in the contiguous United States. Part II: Supercell and QLCS tornado environments. *Wea. Forecasting*, **27**, 1136–1154, https://doi.org/10.1175/WAF-D-11-00116.1.

Trapp, R., and M. Weisman, 2003: Low-level mesovortices within squall lines and bow echoes. Part II: Their genesis and implications. *Mon. Wea. Rev.*, **131**, 2804–2823, https://doi.org/10.1175/1520-0493(2003)131<2804:LMWSLA>2.0.CO;2.

Wakimoto, R., and J. Wilson, 1989: Non-supercell tornadoes. *Mon. Wea. Rev.*, **117**, 1113–1139, https://doi.org/10.1175/1520-0493(1989)117<1113:NST>2.0.CO;2.

——, H. Murphey, C. Davis, and N. Atkins, 2006: High winds generated by bow echoes. Part II: The relationship between the mesovortices and damaging straight-line winds. *Mon. Wea. Rev.*, **134**, 2813–2829, https://doi.org/10.1175/MWR3216.1.

Weiss, J., 1991: The dynamics of enstrophy transfer in two-dimensional hydrodynamics. *Physica D*, **48**, 273–294, https://doi.org/10.1016/0167-2789(91)90088-Q.

Wheatley, D., and R. Trapp, 2008: The effect of mesoscale heterogeneity on the genesis and structure of mesovortices within quasi-linear convective systems. *Mon. Wea. Rev.*, **136**, 4220–4241, https://doi.org/10.1175/2008MWR2294.1.

——, ——, and N. Atkins, 2006: Radar and damage analysis of severe bow echoes observed during BAMEX. *Mon. Wea. Rev.*, **134**, 791–806, https://doi.org/10.1175/MWR3100.1.

Williams, B., J. Allen, and J. Zeitler, 2018: Anticipating QLCS tornadogenesis for decision support: The three-ingredient method during the 19–20 February 2017 south-central Texas tornadic QLCS event. *Major Weather Events and Impacts of 2017*, Austin, TX, Amer. Meteor. Soc., 375, https://ams.confex.com/ams/98Annual/webprogram/Paper331351.html.

Wurman, J., and K. Kosiba, 2013: Finescale radar observations of tornado and mesocyclone structures. *Wea. Forecasting*, **28**, 1157–1174, https://doi.org/10.1175/WAF-D-12-00127.1.

Xu, X., M. Xue, and Y. Wang, 2015: The genesis of mesovortices within a real-data simulation of a bow echo system. *J. Atmos. Sci.*, **72**, 1963–1986, https://doi.org/10.1175/JAS-D-14-0209.1.